Influence of microstructure heterogeneity on the tensile response of an Aluminium alloy designed for laser powder bed fusion

Maxence Buttard, Béchir Chéhab, Charles Josserond, Frédéric Charlot, Pierre Lhuissier, Xavier Bataillon, Alexis Deschamps, Julie Villanova, Marc Fivel, Jean-Jacques Blandin, et al.

▶ To cite this version:

Maxence Buttard, Béchir Chéhab, Charles Josserond, Frédéric Charlot, Pierre Lhuissier, et al.. Influence of microstructure heterogeneity on the tensile response of an Aluminium alloy designed for laser powder bed fusion. Acta Materialia, 2024, 269, pp.119786. 10.1016/j.actamat.2024.119786 . hal-04610418

HAL Id: hal-04610418

https://hal.science/hal-04610418v1

Submitted on 13 Jun 2024

Influence of microstructure heterogeneity on the tensile response of an Aluminium alloy designed for laser powder bed fusion

Maxence Buttard[1], Béchir Chéhab[2], Charles Josserond[1], Frédéric Charlot[3], Pierre Lhuissier[1], Xavier Bataillon[1], Alexis Deschamps[1], Julie Villanova[4], Marc Fivel[1], Jean-Jacques Blandin[1], Guilhem Martin[1*]

1. Univ. Grenoble Alpes, CNRS, Grenoble INP, SIMAP, F-38000 Grenoble

2. Constellium Technology Center, Parc économique Centr'Alp, 725, rue Aristide-Bergès, CS 10027, 38341 Voreppe cedex, France

3. Consortium des Moyens Technologiques Communs (CMTC) - Grenoble INP - Université Grenoble Alpes, BP 75, 38402, St Martin d'Hères, France

4. ESRF – The European Synchrotron, 71 avenue des Martyrs 38043 Grenoble, France

*Corresponding author: guilhem.martin@grenoble-inp.fr

Published in Acta Materialia 10.1016/j.actamat.2024.119786

Abstract

Aluminium alloys designed for additive manufacturing with Zr addition exhibit heterogeneous microstructures from the grain scale down to the atomic scale. Bimodal grain structures with submicron equiaxed grains near the melt pool boundaries and columnar grains at the melt pool interiors are observed. The regions consisting of submicron grains are interconnected in 3D. The tensile response of these alloys often shows the presence of a stress plateau or a yield drop phenomenon near the yield strength but the underlying mechanisms still need to be clarified. Herein we investigate the tensile response of a new Al-4Mn-3Ni-2Cu-1Zr alloy in various conditions: after a stress relief (SR=300°C/4h) as well as after ageing at 400°C for 1h, 4h (peak-aged) and 96h (overaged). Based on the plot of the work hardening rate vs true stress, we identify specific characteristics allowing to appreciate the evolution of the elastoplastic transition depending on the heat treatment. The presence of microyielding and a stress plateau near the macroscopic yield strength are evidenced. Microscale DIC based on the local contrast provided by the microstructure decorated by a high fraction of intermetallic particles turns out to be the relevant scale to clarify the mechanisms involved in the elastoplastic transition. Microyielding is related to the regions near the melt pool boundaries and to the columnar grains. The latter yields at lower stress in comparison with the submicron grains due to a reduced contribution of grain boundary strengthening. The stress plateau is attributed to the low work-hardening capacity of the submicron grains.

Keywords: Mechanical response; 3D microstructure; Aluminium alloys; Additive Manufacturing

1. Introduction

High-strength aluminium alloys from the 2XXX [1], 6XXX [2], [3], and 7XXX series [4], [5] are challenging to process using L-PBF due to the development of hot cracks. The main solution to overcome hot cracking issues consists in refining the grain size to distribute thermal stresses over a larger number of interfaces. Different strategies have been proven to be efficient in promoting the heterogeneous nucleation of the Al grains to increase the density of interfaces. Successful attempts of mixing the Al alloy powder with extra particles such as TiB_2 [6], [7], or CaB_6 [8] have been reported in the literature. However, the most widely used strategy consists in introducing into the nominal composition elements known to precipitate the primary $L1_2$-Al_3X phase (X = Zr [9]–[14], Sc [12], [15]–[17], Ti [18], [19], Nb [20], [21], Ta [22]). The $L1_2$-Al_3X phase is a very efficient grain refiner because of its very low misfit in the lattice parameter in comparison with the FCC Al phase. The latter strategy is certainly the most straightforward (preliminary mixing stage suppressed) and was exploited by many authors interested in designing new high-strength alloys for additive manufacturing, see e.g. [9], [11]–[13], [23]–[26]. When the strategy aiming at promoting the heterogeneous nucleation of Al grains onto primary $L1_2$-Al_3X precipitates is deployed, the as-fabricated material shows a bimodal grain structure with regions consisting of fine grains (FZ) near the melt pool boundaries (MPBs) and regions made of coarser grains (CZ) at the melt pool center [9], [15], [27]. The mechanisms responsible for such a bimodal grain structure have been recently clarified [9]–[11], [25], [28]. The solid-liquid interface velocity is found to be a key parameter. At the MPBs, the solid-liquid interface velocity is low enough to allow the precipitation of the $L1_2$-Al_3X primary phase. On the contrary, when approaching the melt pool center, the solid-liquid interface velocity increases, and the nucleation of the primary phase is suppressed. The element X (often a slow diffuser in Aluminium) is thus retained in solid solution in the region made of coarser grains. Such variations in solidification conditions at the melt pool scale may also affect the morphology of the second-phase particles forming in the last stage of solidification and the composition of the supersaturated solid solution, see [15], [27], [29].

Some authors have recently attempted to characterize the room-temperature mechanical behaviour of the heterogeneous microstructures of Al alloys processed by L-PBF at the melt pool scale. In alloys with a substantial volume fraction of eutectic without the addition of solute X=Ti, Sc, Zr, known to refine the grain size due to the precipitation of the primary $L1_2$-Al_3X, the regions near the MPBs are reported to be softer than the melt pool interiors (MPIs) [30]–[32]. For example, Otani *et al.* [30] performed in situ tensile tests in the SEM and measured the strain distribution at the melt pool scale using digital image correlation (DIC) in an as-printed Al-12Si eutectic alloy. The most deformed regions were systematically located near the MPBs. They concluded that the regions close to MPBs are local soft regions. The underlying mechanisms leading to these soft regions near the MPBs were not discussed. Fite et *al.* [31] studied the inhomogeneous deformation of the as-printed AlSi10Mg alloy and established some correlation with local microstructure. Regions near the MPBs were found to yield sooner than the MPIs. Earlier yielding near MPBs was correlated to the presence of a coarser microstructure with larger cells and a more discontinuous network of second-phase particles in comparison with the MPIs. Ajantiwalay *et al.* [32] have investigated the influence of microstructural heterogeneities on the small-scale mechanical properties in an Al-10.5Ce-3.1Ni-1.2Mn alloy fabricated by L-PBF and subjected to a stress-relief heat treatment at 450°C for 2h. Nanoindentation and micro-pillar compression were used and the regions near the MPBs were found to be the weak spots in the microstructure (lower yield strength in comparison with the MPIs) because of a locally coarser intermetallic network.

In alloys containing significant additions of Ti, Sc, or Zr, submicron fine equiaxed grains are found near the MPBs. Such regions are reported to be harder than the MPIs. Haridas *et al.* [33] and Dhal *et al.* [34] have used nanoindentation mapping at the melt pool scale to determine the local distribution in hardness in the as-printed Al-3Ni-1Ti-0.8Zr alloy. In both studies, the regions near MPBs and consisting of fine equiaxed grains were found harder than the MPIs. This difference was attributed to the presence of a larger proportion of hard intermetallic particles. Dhal *et al.* [34] proposed that the primary precipitates of the $Al_3(Ti, Zr)$ phase at the center of aluminium grains are responsible for the high hardness values measured near the MPBs, such precipitates being absent in the regions consisting of coarser grains in the MPIs. Haridas *et al.* [33] highlighted the role of the Al_3Ni phase to account for the hardness increase near the MPBs. Surprisingly, the authors did not establish possible correlations between the local variations in hardness and local changes in grain size or solid solution composition. Bayoumy *et al.* [27] investigated the micromechanical behaviour of the bimodal grain structure of an Al-Mn-Sc alloy processed by L-PBF and heat-treated at 300°C for 6h (peaked-aged). They studied the mechanical behavior of different regions of the microstructure using micro-tensile specimens extracted from specific regions of interest using FIB. Differences in mechanical behavior were revealed when comparing the fine-grained region with the region consisting of coarser grains. The micro-tensile tests showed that the fine-grained regions were harder and less ductile than the coarse-grained regions [27]. Grain boundary strengthening was invoked to account for the higher hardness of the fine-grained regions compared to those consisting of coarser grains. The micro-tensile tests also revealed a difference in work-hardening capacity between the regions made of fine and coarse grains. To summarize, all those pioneering works [27], [30]–[34], lead us to consider the composite nature of the microstructure of high-strength Al alloys designed for and fabricated by L-PBF.

In this contribution, the evolution of the tensile response upon ageing at 400°C of a new Al-4Mn-3Ni-2Cu-1Zr alloy designed for and fabricated by L-PBF is investigated with a particular emphasis on the elastoplastic transition. The microstructure inherited from L-PBF shows a bimodal grain structure with fine grains near the MPBs and coarser columnar grains at the center of the solidified melt pool. The 3D characterization of the microstructure using synchrotron X-ray nanotomography (nano-CT) and machine learning-assisted segmentation reveals the 3D percolation of the fine-grained regions. Specific features such as micro-yielding and the presence of a stress plateau are identified in the macroscopic tensile stress-strain response. Finally, the mechanisms responsible for those specific features are clarified using in situ tensile tests conducted in the SEM coupled with microscale digital image correlation (DIC). The key role played by the fine-grained regions on the resulting tensile response is emphasized and discussed.

2. Experimental Procedures

2.1. Materials and heat treatments

The material of interest is an Al-4Mn-3Ni-2Cu-1Zr (in wt.%) alloy designed for and processed by L-PBF using an EOS M290 L-PBF machine operating under high-purity argon (< 0.2% O_2). Powder characteristics (morphology, size) and L-PBF processing conditions are as follows: D50 = 43 µm preheating temperature (set to 100°C), laser power (370 W) and speed (1600 mm/s), spot size (70 µm), layer thickness (60 µm); more details can be found in [25], [35], [36]. The lasing strategy uses 4 mm stripes with a snake-like scanning pattern rotated by 67° between each layer. The distance separating two adjacent tracks, often called hatch distance was set to 140 µm. Cylindrical (diameter = 11 mm and height = 60 mm) and wall samples ($11\times60\times60$ mm^3) were fabricated, the largest dimension being parallel to the build direction.

Samples were all subjected to a Stress Relief (SR) heat treatment at 300°C for 4 hours before being removed from the building plate. Following the SR heat treatment, samples were aged at 400°C to further increase the material strength through precipitation strengthening [36]. Four conditions summarized in **Table 1** and corresponding to different aging times are examined in this work: the SR is taken as the initial condition, the SR+400°C/1h is slightly underaged, the SR+400°C/4h is peak-aged, and the SR+400°C/96h is overaged.

Heat Treatment	Temperature (°C)	Time (hours)
Stress Relief (SR)	300	4
SR+ 400°C/1h	400	1
SR + 400°C/4h	400	4
SR + 400°C/96h	400	96

Table 1 : Summary of the different heat treatments investigated.

2.2. Microstructure characterization

2.2.1. SEM and EBSD

Samples were prepared using standard polishing procedures: SiC abrasive papers down to the P4000 grade, followed by two steps using successively a 3µm and 1 µm diamond suspension. A final vibratory polishing with a VibroMet device from Buhler was conducted for 4h prior to microstructural observations using a 0.03µm colloidal silica suspension. The grain structure was analyzed using Electron Backscattered Diffraction (EBSD) in a Zeiss Gemini SEM 500 FEG microscope. Large maps were collected using a 200 nm step size. Maps in the FZ were acquired using a 50 nm step size. Both the backscattered electronic (BSE) and secondary electronic (SE) imaging contrasts were employed to collect micrographs to investigate the microstructure at the melt pool scale.

2.2.2. Synchrotron X-ray Nanotomography

To get a better idea of the microstructure in 3D, in particular of the 3D arrangements of regions consisting of different microstructures, nano-CT was carried out at the ID16B beamline at the European Synchrotron Radiation Facilities (ESRF). Using a Kirkpatrick-Baez (KB) pair of mirrors, a 29.6 keV X-ray beam was focused down to a nanobeam (50×50 nm^2). The focused beam acts as a secondary source for a conic beam. A PCO Edge 5.5 sCMO Camera (2560×2160 pixels) was positioned downstream from the secondary source at a predetermined distance. Therefore, multiple fields of view and subsequently different magnifications can be selected by altering the sample position between the secondary source and the detector. An effective pixel size of 88.4×88.4 nm^2 was chosen for the measurements performed in this work.

The camera field of view was artificially increased: (i) horizontally by using the so-called half-acquisition method with a position offset of the rotation axis of 700 pixels (over 2560), (ii) vertically by concatenating four tomographic scans acquired on top of each other along the vertical axis of the sample with a field of view (FOV) overlap of 400 pixels. From the aligned raw images, phase contrast was retrieved using an algorithm based on the Contrast Transfer Function method [37]. The final volume was reconstructed from those phase images using filtered back projection with the ESRF software PyHST2 [38].

2.2.3. Automated segmentation of 3D images assisted by Artificial Intelligence

Segmenting the 3D images to identify different microstructures within a large data set (nearly 300×300×300 μm^3) in a reasonable timeline was found to be very challenging if not impossible using traditional image analysis procedures. To facilitate and speed up the segmentation, an Artificial Intelligence (AI) algorithm can be trained on subvolumes extracted manually from large 3D datasets. A random forest algorithm with 200 trees and a maximum depth of 30 was trained on pre-processed data. To make the training possible in a reasonable time, several features were calculated for each voxel to characterize the local environment based on the local gray contrast. More details regarding the AI-assisted image analysis used in this work are given in **Appendix A**.

When the accuracy of this AI was considered good enough, it was applied to larger volumes. One of the most challenging parts is the automation of this workflow since the raw data sets are relatively big (about 100 Go). The segmented image can then be labeled to point out the isolated zones in the microstructure. Finally, the 3D views are generated using the Avizo Software.

2.4 Mechanical characterization

2.4.1. Macroscopic tensile tests

Cylindrical tensile specimens whose geometry and dimensions are given in supplementary materials (*Figure S 1a*), were machined from L-PBF cylindrical specimens. Tensile tests were carried out using an MTS4M testing machine equipped with a 20kN cell force. Tests were conducted at a constant strain rate $\dot{\varepsilon} = 10^{-4}$ s^{-1} and the loading direction was parallel to the build direction. Prior to testing, the gauge length of the tensile specimens was first covered with a white painting. A speckle made of fine droplets of black painting was then deposited. Macroscale digital image correlation (GOM software) was employed to record the strain fields and measure the deformation throughout the tests. Two 6M-pixel cameras were used and the frequency of acquisition of the images was set to 2 Hz. The yield strength (YS) was determined by measuring the true stress at 0.2% plastic strain.

2.4.2. In-situ tensile test and microscale strain distribution

Mini-tensile specimens were extracted from the wall samples using electron discharge machining for conducting in situ tests in the SEM. The specimens were machined so that the gauge length was parallel to the build direction. The geometry and dimensions of the mini-tensile specimens are given in supplementary materials, see *Figure S 1*. Prior to testing, the specimens were mirror-polished with a 0.03µm-solution of colloidal silica so that images of the microstructure can be collected using SEM. Tensile tests were carried out in a ZEISS Gemini SEM500 using a Deben MT2000 EW micromechanical device controlled with a homemade LabView interface to impose a constant strain rate of 10^{-3} s^{-1}. High-definition (HD, 8192×6459 pixels) BSE images of the same region of interest were collected after different strain increments using a 15 kV acceleration voltage. This enables monitoring a relatively large field of view containing several melt pools while preserving a good definition (pixel size of 29 nm). Here, the local contrast provided by the microstructure, in particular by the large fraction of relatively fine intermetallic particles is exploited to determine the microscale strain distribution using DIC. DIC was performed using the CMV software [39]–[41]. A region of interest (ROI) was selected in the HD-BSE image of the undeformed configuration. The ROI was then subdivided into subsets of 40×40 pixels (1.2×1.2 µm). With such a subset size, the objective was to determine the strain distribution at the scale of the FZ and CZ. The subsets were then overlaid onto the HD-BSE image and each subset was associated with a color: blue for the FZ and green for the CZ based on the local morphology and distribution of the intermetallic particles. An example is provided in supplementary material, see *Figure S 2*. This step was done manually and was time-consuming but is only required for the undeformed image since the belonging of the different subsets to the FZ or CZ can then be updated in the deformed images. As a result, the exact position of the boundaries suffers from the discretization of the ROI into subsets for subsequent DIC analysis. Given the size of the subset with respect to the typical size of the FZ and CZ, this was considered reasonable to determine the strain distributions within the FZ and CZ.

The local strain measurements obtained by DIC were then post-processed using in-house Python routines developed specifically for this work.

3. Experimental Results

3.1. Overview of the microstructure

Figure 1a illustrates the bimodal grain structure in the SR conditions with the presence of fine equiaxed zones (FZ, black regions in **Figure 1a**) along the MPBs, see a typical SEM-BSE image in **Figure 1b**, and zones consisting of coarser columnar grains (CZ) in the melt pool center, see an example in **Figure 1c**. The FZs are mostly displayed in black in **Figure 1a** because it was not possible to properly index the matrix using a 200 nm step size in the presence of such a high fraction of intermetallic particles. The grain size in the FZ, measured in previous works [35], [36] based on the definition of the equivalent diameter from crystallographic orientation maps collected using ACOM (Automated Crystallographic Orientation Mapping) in the TEM with a 15 nm step size, is about 500 nm. This estimate of grain size in the FZ is consistent with the EBSD map shown as inset in **Figure 1a**. The fraction of FZ was estimated to be about 35 ± 5%. This was estimated by taking the unindexed black regions and by applying a criterion on the sphericity of the indexed grains: grains with a sphericity index < 0.35 are classified as columnar grains. Regardless of the region of interest, FZ or CZ, the texture is relatively weak [35]. **Figure 1b-c** recall that the microstructure in both FZ and CZ is decorated by a high fraction of relatively fine intermetallics (roughly 20% with a size between 100 and 500 nm) regardless of the regions of interest. The nature of the various intermetallics was identified in our previous work based on XRD coupled with nanodiffraction and EDS in the TEM, see [36] for more details. The morphology of those intermetallics is globular in the FZ (**Figure 1b**) and more elongated in the CZ (**Figure 1c**) [36]. The effect of ageing time at 400°C on the microstructure has been described in detail in [36]. After 1h and 4h at 400°C, there are only minor variations of the grain structure (*Figure S 4a* and *Figure S 5a)* and of the intermetallic population (*Figure S 4b-c* and *Figure S 5b-c*). The most important microstructural evolutions take place at the nanoscale because of the decomposition of the supersaturated solid solution, especially in Zr and Mn that goes along with the formation of both spherical $L1_2$-Al_3Zr precipitates and plate-like $Al_{60}Mn_{11}Ni_4$ precipitates. After a long time of exposure at 400°C (96h), the grain structure does not undergo significant variations (*Figure S 6a*) but some of the intermetallic particles, those enriched in Cu and Ni, have substantially coarsened (*Figure S 6b-c*), especially in the FZ (*Figure S 6c*). At the nanoscale, the spherical $L1_2$-Al_3Zr nanoprecipitates have coarsened and eventually transformed into their most stable form D023-Al_3Zr. The interested reader is referred to [36] for more details regarding the microstructural evolutions induced by ageing at 400°C.

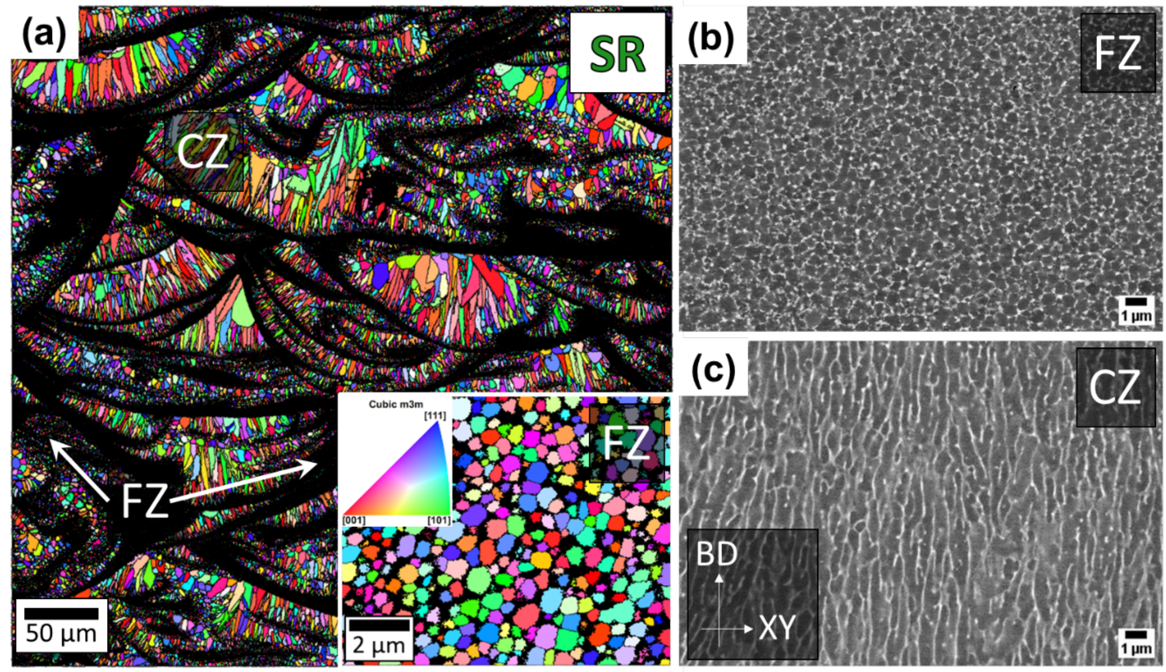

Figure 1: Overview of the microstructure in the SR conditions. (a) Low-magnification EBSD-IPF map of aluminium revealing the bimodal grain structure with fine equiaxed zones (FZ, mostly in black) and zones consisting of coarser columnar grains (CZ) – step size = 200 nm reproduced from [36]. The inset is an EBSD-IPF map collected in the FZ with a 50 nm step size. Typical examples of BSE images taken respectively in the (b) FZ, and (c) CZ. Intermetallic particles appear in bright contrast.

Interestingly, one can find a way to cross the entire EBSD map along the X/Y or Z-axis by going through the black regions (FZs). The latter observation suggests that the regions consisting of fine equiaxed grains are percolating across several melt pools. In other words, regions consisting of coarse columnar grains can be considered embedded in a matrix made of fine equiaxed grains. Because this idea can be of utmost importance from a mechanical viewpoint, the 3D arrangement of the FZ and CZ in a region of interest containing multiple melt pools was characterized to verify the 3D nature of the percolation of the FZs. This is achieved using synchrotron nano-CT.

3.2. 3D arrangement of the FZs and CZs

Nano-CT enables the 3D observation of a region of interest of nearly 300×300×300 μm^3 including several melt pools. The analysis is performed on a sample taken in the SR conditions but the insights gained for such a 3D analysis can be used for samples aged at 400°C because no major variation of the grain structure was detected after 400°C/96h (*Figure S 6a*). A typical cross-section extracted from the reconstructed volume is shown in **Figure 2a**. The phase contrast helps to distinguish the interfaces between the FZs and CZs. Multiple melt pools can be identified in **Figure 2a**. The two zones can be discriminated simply based on the local texture (local variations in grayscale) induced by the intermetallics as illustrated in **Figure 2b** where an enlarged view of the black box drawn in **Figure 2a** is shown. An automated segmentation allowing the distinction between the FZ and the CZ in 3D in such a large volume turns out to be very challenging using conventional segmentation procedures. Thus, we developed an AI-assisted image segmentation to identify FZs and CZs in large datasets ($300 \mu m^3$). Results are shown in **Figure 2c** and **Figure 2d** for respectively the CZs and the FZs in a SR sample. The volume fraction of FZ resulting from the segmentation procedure is about

39%. This is in relatively good agreement with the value derived based on low-magnification EBSD maps (35 ± 5%) such as the one displayed in **Figure 1a**. Because our goal is to confirm our hypothesis that the FZ is percolating in 3D and the CZ is not, each isolated region was represented using a different color. **Figure 2c** shows only the CZs. It is not possible to find a color that crosses the whole region of interest along the X/Y direction or the build direction suggesting that the CZ is not percolating. On the contrary, the FZs are interconnected both horizontally along the X/Y direction and vertically along the build direction. This is clearly illustrated in **Figure 2d** where the reddish region can be seen as the matrix. Note that the 3D view shown in **Figure 2d** may suggest that the FZ is present in larger proportion than the CZ but this is an artifact caused by the 3D rendering. An example of a 2D slice extracted from the 3D image along with its segmented counterparts is given in supplementary materials, see *Figure S 3*. Based on this 3D analysis across multiple melt pools, it is reasonable to consider that CZs are embedded in the matrix made of FZs.

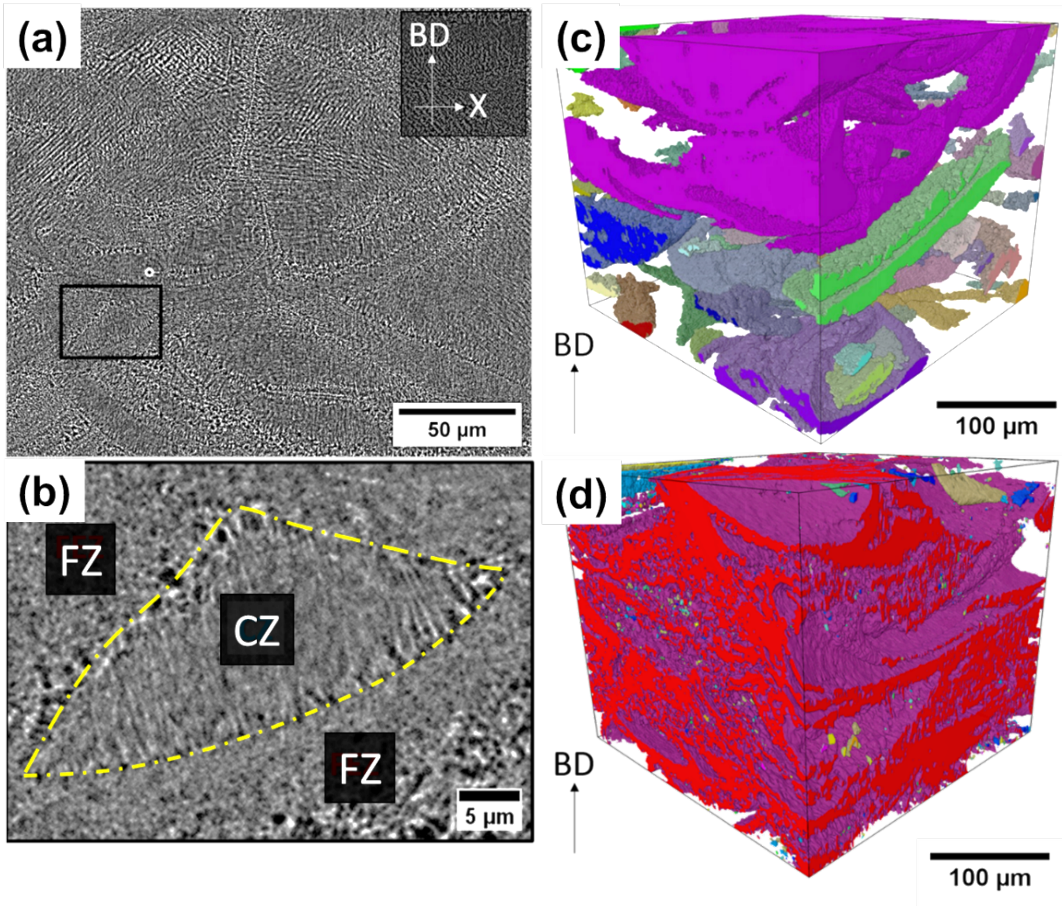

Figure 2: 3D characterization of the microstructure of a sample in the SR conditions using nano-CT (voxel size = 100 nm^3). Example of a sample taken in the SR conditions. (a) 2D cross section extracted from the reconstructed 3D image revealing the presence of several melt pools within the region of interest. (b) Enlarged view of the black box drawn in (a). Intermetallic particles appear in white and the aluminium in gray. The output of the AI-assisted image analysis is given respectively for both the CZs and FZs in (c) and (d). Each color corresponds to an isolated object.

3.3. Evolution of the tensile response with the ageing time at 400°C

Figure 3a shows the macroscopic true stress-true strain tensile response of samples aged at 400°C. In the SR conditions, the yield strength taken at 0.2% of plastic strain (denoted here YS) is about 330 MPa and ultimate tensile strength (UTS) is equal to nearly 470 MPa giving a work-hardening capacity defined as $\Delta\sigma_{WH}$ = UTS – YS equal to 140 MPa. Both YS and UTS increase during the first four hours at 400°C reaching respectively 430 and 500 MPa after 400°C/4h. This goes along with a decrease in work-hardening ($\Delta\sigma_{WH}$ = 70 MPa). After 400°C/96h, both YS and UTS decrease respectively down to 300 and 350 MPa further decreasing the work hardening capacity ($\Delta\sigma_{WH}$ = 50 MPa).

The evolutions of the shape of the tensile curves with the ageing time can be seen in **Figure 3a**. In particular, the samples aged at 400°C show the presence of a stress plateau near the YS. To investigate in more detail the elastoplastic transition in the various conditions studied in this work, the quantity $\frac{\partial \ln(\sigma)}{\partial \ln(\varepsilon)}$ is plotted in **Figure 3b** as a function of true stress, and in **Figure 3c** as a function of true strain. It allows the local changes in work-hardening behaviour to be highlighted. A first change pointed out using black arrows in **Figure 3b** is detected in the SR sample as well as in the SR+400°C/1h and SR+400°C/4h while this local change in work-hardening seems to be absent in the SR+400°C/96h sample. Throughout this manuscript, this peculiar characteristic associated with a non-linear decrease in the work-hardening rate is defined as the micro-yield strength (MYS). From **Figure 3b**, another observation can be made: the derivative does not continuously decrease with increasing true stress. Beyond a point highlighted using blue arrows in **Figure 3b**, the value of the local derivative increases. This particular characteristic will be referred to as the inflection point (IP) throughout this work. Note that this IP is observed regardless of the ageing time at 400°C. The IP occurs at a given strain regardless of the ageing time, see **Figure 3c**. The evolutions of the YS and UTS with ageing time are reported in **Figure 3d** using square and star symbols respectively and permit us to appreciate the evolution of the work-hardening capacity upon ageing at 400°C. The evolution of the two characteristic points identified in **Figure 3b**, namely the MYS, and IP, are given in **Figure 3d** which also reflects the ageing response of the investigated material. The peak-aged condition is reached in the SR+400°C/4h sample while the sample SR+400°C/1h is slightly underaged, and the sample SR+400°C/96h is overaged, see **Figure 3d**. The differences between the MYS and YS, and between the YS and IP decrease during the first four hours of ageing at 400°C.

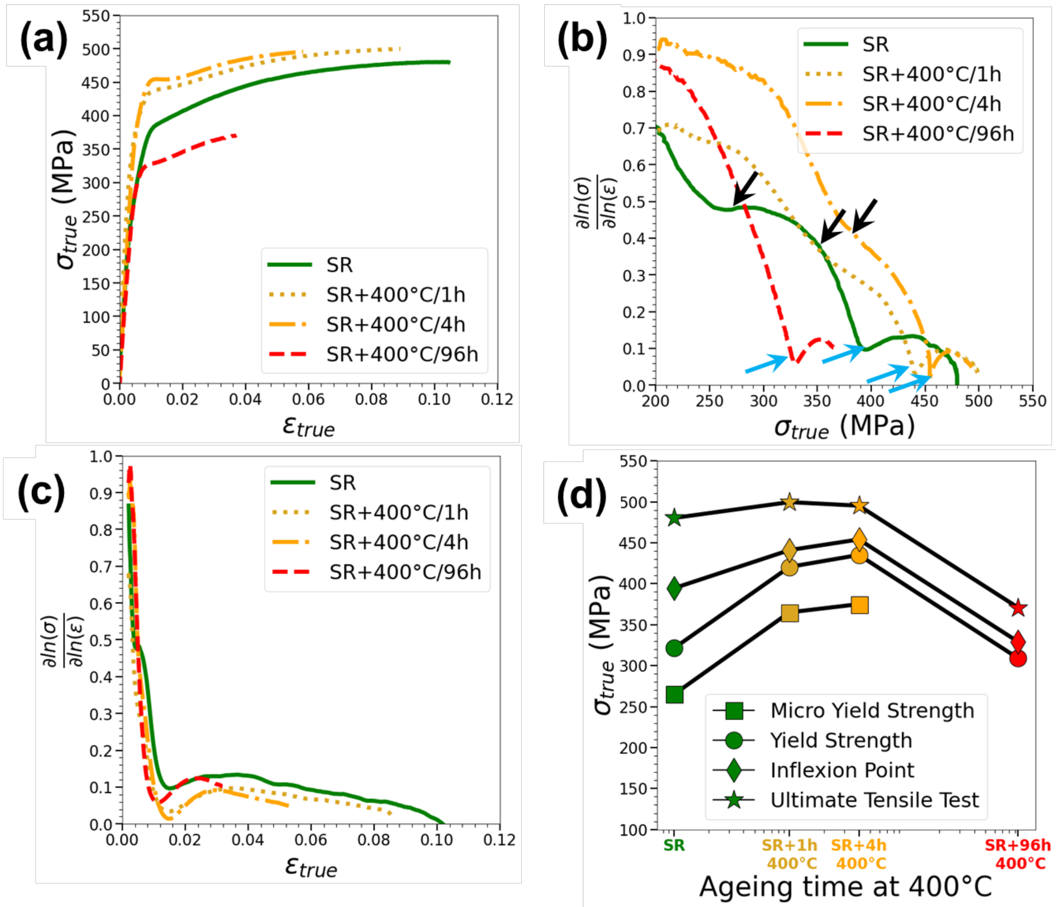

Figure 3: (a) Evolution of the true stress-true strain tensile response with the ageing time at 400°C. Logarithmic derivative of the tensile response versus (b) true stress, and (c) true strain. Black arrows in (b) point out the micro-yield strength (MYS) while the blue arrows indicate the inflection point (IP) for each condition in (b) and (c). (d) Evolution of the MYS, YS, IP and UTS as a function of ageing time at 400°C. The black cross symbols are associated to specific stress values selected to plot the macroscale and microscale strain fields shown in section 3.4 and 3.5.

3.4. Macroscale digital image correlation

To gain further insights into the mechanisms involved in the elastoplastic transition as well as the origin of the MYS and the stress plateau, the strain fields recorded during the macroscopic tensile tests using macroscale DIC are examined. For sake of clarity, we focus hereafter only on the result of the SR+1h/400°C for which the stress plateau is directly evidenced in the macroscopic tensile response. The macroscopic tensile response of the SR+400°C/1h sample, where the YS and UTS as well as the two characteristic points (MYS and IP) are indicated, is shown in **Figure 4a**. Three tensile strain fields of the entire gauge length of the tensile specimen are displayed in **Figure 4b-d**. The full video showing the evolution of the strain fields upon straining for the SR+400°C/1h sample is provided in supplementary materials, see **Video 1**. The first strain field shown in **Figure 4b** was deliberately extracted for a given tensile stress between the MYS and the YS (typically ~380 MPa). The second strain field was taken after the YS but before the inflection point (~430 MPa), see **Figure 4c**. Finally, the third strain field (**Figure 4d**) was extracted after the inflection point (~450MPa). The strain fields are relatively homogeneous with no sign of strain localization. Besides, no trace of plastic instability involving the propagation of deformation bands could be evidenced at this scale. The same conclusion can be drawn for other samples subjected to different ageing times. The videos showing the evolution of the macroscale strain distribution upon straining are given in supplementary materials for the SR (**Video 2**), SR+400°C/4h (**Video 3**), and SR+400°C/96h (**Video 4**). The position of MYS, YS, and IP on the tensile response of the various microstructures studied is given in the video stills of **Video 1**-**Video 4**. Further investigations at a finer scale are thus required to clarify the origin of the MYS and the stress plateau.

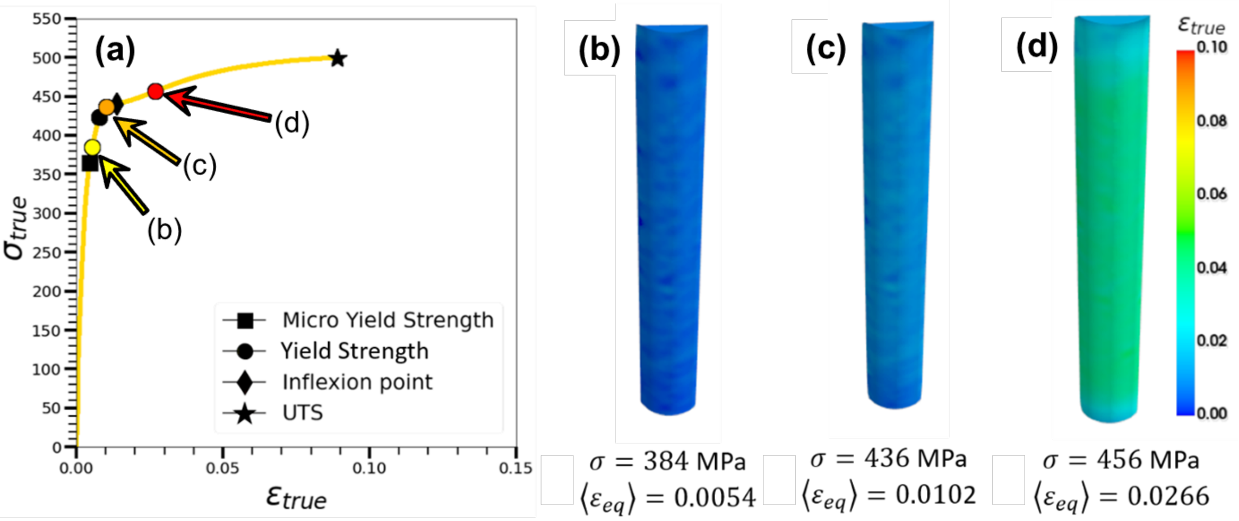

Figure 4: (a) True stress-strain curve for the SR+400°C/1h sample (black curve). The characteristic points identified previously are reported here as references using the same symbols used in Figure 3d. Macroscopic strain fields over the entire gauge length of the tensile specimens are given for three different levels of stresses: (b) between MYS and YS, (c) between YS and IP, and (d) beyond IP.

3.5. Development of microscale strain heterogeneities

As recalled in **Figure 1**, the microstructure is highly heterogeneous at all scales. The 3D arrangement of the FZs and CZs revealed in **Figure 2** and the relative mechanical behaviour of each zone may have an impact on the resulting mechanical response. To clarify the mechanisms at the origin of the MYS and the stress plateau, in situ tensile tests were conducted in the SEM and high-definition images were collected after different tensile strain increments. DIC was employed to determine the microscale strain distribution. This approach enables the establishment of some correlations between the local strain heterogeneities and the underlying microstructures. It was first verified that the tensile response measured using flat dog-bone mini-tensile specimens is similar to the one register during tensile testing using cylindrical macro-tensile specimens. The macroscopic stress was calculated from the force recorded at each step of deformation, and the strain was taken as the average tensile strain calculated over the entire ROI selected for microscale DIC. An example is given in supplementary materials, see *Figure S* 7. Once again, the example of the SR+400°C/1h sample is taken in the subsequent sections for the sake of clarity. When differences or similarities are found in comparison with the other conditions, they are emphasized and illustrated.

3.5.1. Onset of plastic deformation

Figure 5a displays the microscale strain distribution for a given macroscopic tensile stress taken above the MYS but below YS for the SR+400°C/1h sample. All the FZ/CZ interfaces have been highlighted in black and the regions associated with the CZ are hatched. This analysis aims at investigating the origin of the MYS through the examination of the onset of plastic deformation.

Upon close examination of the microscale strain fields displayed in **Figure 5a**, regions where plastic deformation starts are identified. The line crossing vertically the strain map is an imaging artifact causing a displacement revealed by DIC and thus should be ignored. Most regions involved in the onset of plastic deformation appear to be located in the CZ (see examples pointed with gray arrows) or near the FZ/CZ interfaces at the MPBs but preferentially on the CZ side, see examples of such regions pointed with black arrows in **Figure 5a**. Finally, a few regions subjected to plastic strain initiation are also found within the FZ, see two examples pointed with white arrows in **Figure 5a**. The tensile strain probability distribution functions in the entire ROI as well as in the FZ and CZ taken at the same level of macroscopic tensile stress as the strain map shown in **Figure 5a** are given in **Figure 5b**. The x-axis is the normalized tensile strain, i.e. $\varepsilon_{11}/\varepsilon_{11}^{macro}$, where ε_{11}^{macro} is the average tensile strain computed over the entire strain map. From **Figure 5b**, it can be confirmed quantitatively that the most strained regions are preferentially located in the CZ: at large strains, the strain distribution in the CZ (blue dotted line) overlaps that of the strain distribution in the entire ROI (full gray line). Similar observations can be made in the SR sample (*Figure S 8a*) and to a lesser extent in SR+400°C/4h sample (*Figure S 9a*) for a macroscopic stress taken between MYS and YS. However, the case of the SR+400°C/96h is different: the initiation of plastic deformation is not necessarily found to occur in the CZ or near the FZ/CZ interfaces located at the bottom of the FZ, see *Figure S 10a*.

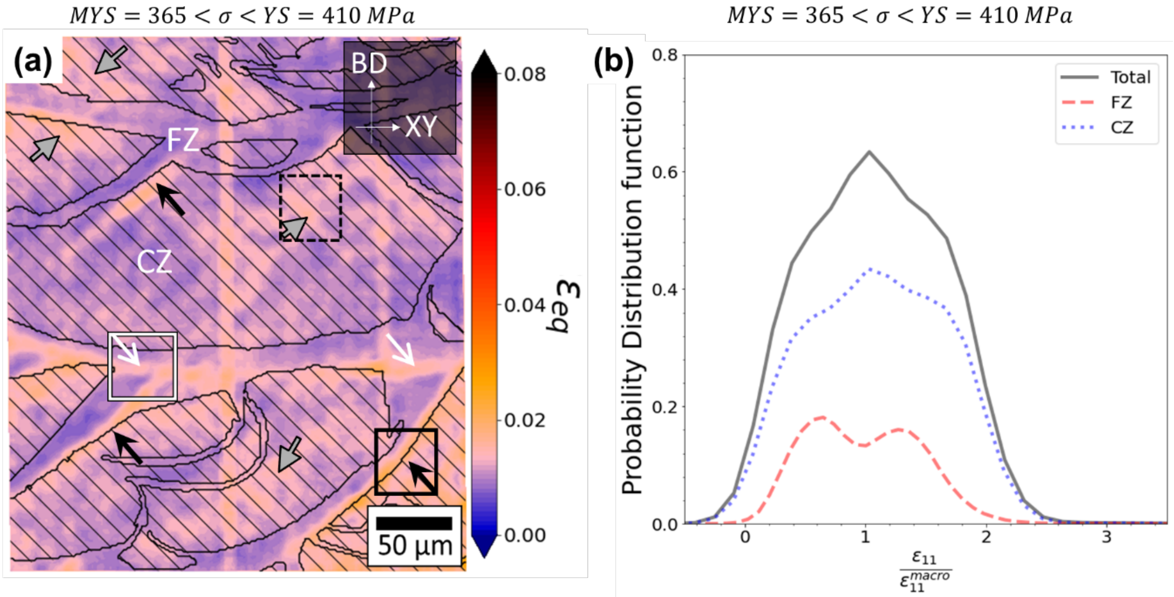

Figure 5. (a) Microscale strain field in the SR+400°C/1h sample determined using DIC for a given macroscopic tensile stress between the MYS and the YS. The hatched areas represent the CZ while the others are associated with the FZ. The gray arrows highlight regions located within the CZ and subjected to plastic strain initiation. The black arrows highlight regions of interest subjected to strain localization at the CZ/FZ interfaces. The white arrows point to regions affected by strain localization within the FZ. The black lines correspond to the interfaces between FZ and CZ. (b) Probability distribution functions in the entire ROI and in the FZ and CZ respectively vs. the normalized tensile strain.

In the SR+1h/400°C sample, the regions where plastic deformation initiates are now further investigated using SEM. Typical examples of BSE images taken in those regions and corresponding to the black, white, and dashed black boxes drawn in **Figure 5a** are shown in **Figure 6a-f**. In the region of interest corresponding to an FZ/CZ interface associated with a MPB (black box in **Figure 5a**), local microstructural changes are hardly distinguishable at this scale, see **Figure 6a-b**. Similarly, SEM observations in the FZ (white box in **Figure 5**) where plastic deformation starts do not reveal striking local changes in microstructure – at least at this scale - see **Figure 6c-d**. Interestingly, the early stage of plastic deformation observed in the CZ is punctually associated with a specific microstructural characteristic: the presence of twin dendrites, see the example delineated using green dashed lines in **Figure 6e**. The mirror twin plane separating the dendrite primary trunk is highlighted using the white dotted line in **Figure 6e-f**. Such twin dendrites are recognizable by their specific feather-like morphology [42]–[44] but the presence of twin dendrites in this alloy was previously reported and the existence of a twin plane was verified based on orientations maps collected using ACOM [35]. Interestingly, twin boundaries were recently identified as interfaces sensitive to strain localization [45], [46].

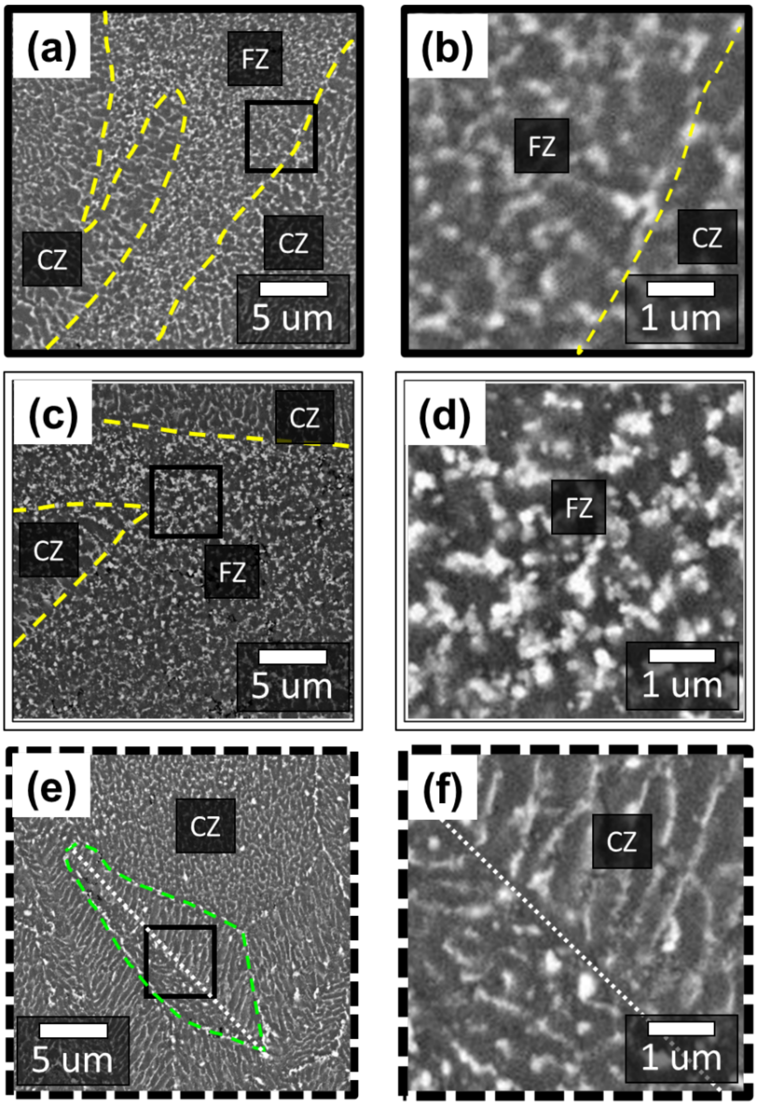

Figure 6: Examples of BSE images taken at different magnification in the regions of interest where the onset of plastic deformation was detected. (a,b) at the FZ/CZ interface associated with the MPB, (c,d) within the FZ, and (e,f) at the twin boundary of twin dendrite in the CZ. The dashed yellow lines represent the interface between the two zones. The white dotted line in (e) highlights the twin plane while the green dashed lines highlight the twin dendrite. Those images were taken for a macroscopic tensile stress between the MYS and YS.

3.5.2. Evolution of the microscale strain distribution during tensile loading

The evolution of the local plastic strain distribution during tensile deformation is first examined qualitatively by looking at microscale strain fields extracted after different strain increments associated with different levels of macroscopic tensile stresses, see **Figure 7a-f**. Such strain maps reveal the local plastic deformation heterogeneities and their evolution upon straining. The strain map shown in **Figure 5a** and corresponding to a level of macroscopic stress just above MYS is reproduced using a different color scale in **Figure 7a**. When the macroscopic tensile stress approaches the macroscopic YS, the CZ seems to carry more deformation than the FZ, see **Figure 7b**. Between YS and IP, both CZ and FZ appear to be plastically deformed but the less strained regions are preferentially located in the FZ, see the regions displayed in purple in **Figure 7c**. When approaching the IP, plastic deformation within the FZ becomes more homogeneous, see **Figure 7d**. Beyond the IP, strain localization starts in the FZ as shown in

Figure 7e. For larger macroscopic strains, the strain localization in the FZ is even more pronounced, see **Figure 7f**. The full sequence of the strain fields recorded during the in situ tensile test can be seen in **Video 5**.

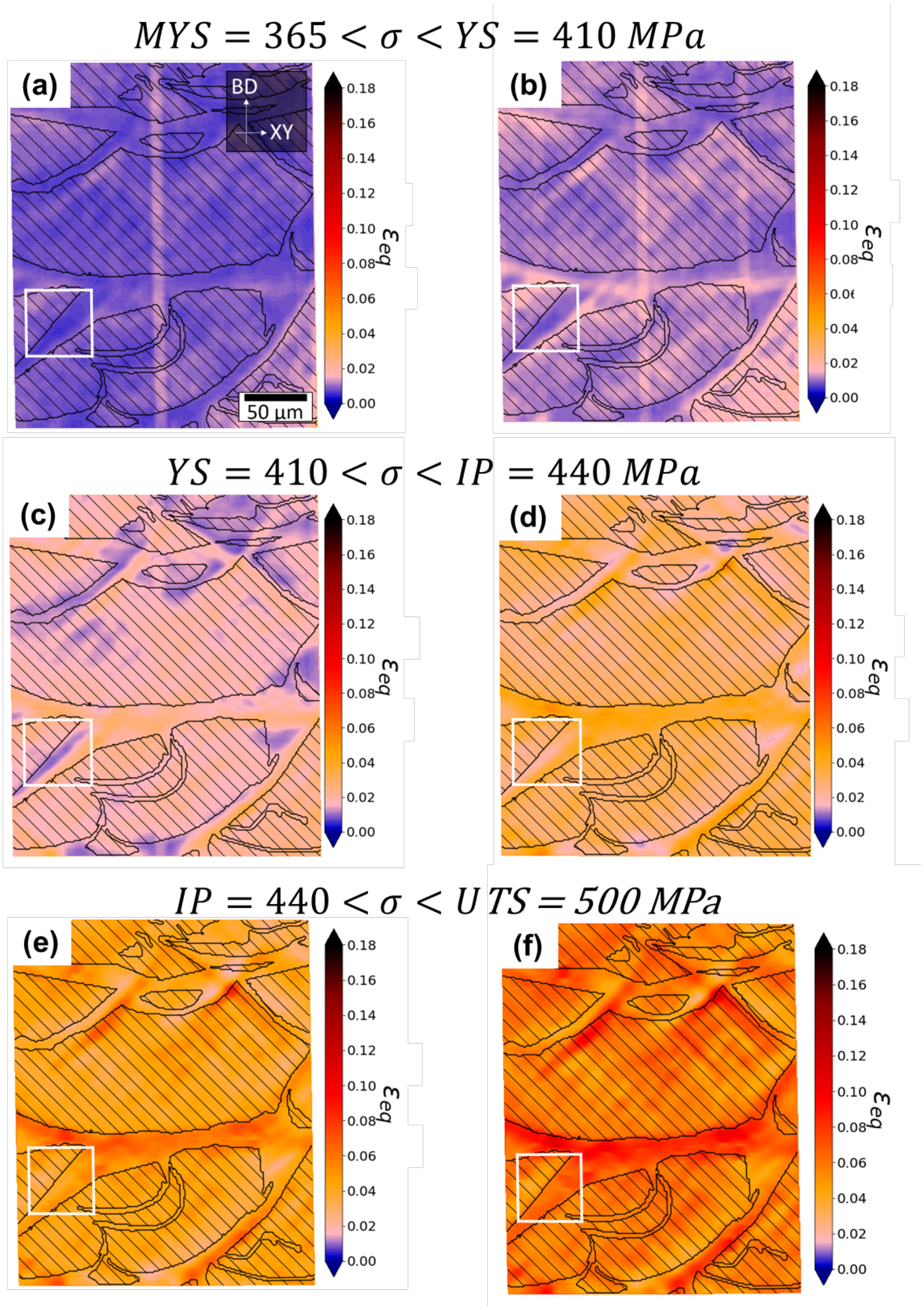

Figure 7: (a-d) Microscale strain fields determined in the SR+400°C/1h sample using DIC for different levels of macroscopic tensile stress: (a-b) MYS < σ < YS; (c-d) YS < σ < IP; and (e-f) IP < σ < UTS. The black lines correspond to the interfaces between FZ and CZ. The CZ is identified as the hatched areas.

To achieve a more quantitative description of the evolution of the strain partitioning between the CZ and the FZ during tensile deformation, the normalized tensile strain distributions within each zone and that computed over the entire ROI are plotted in **Figure 8a-f**. For macroscopic stresses beyond the MYS but below the YS, the strain distribution in the CZ (dotted blue line in **Figure 8a**) and the overall strain distribution (gray full line in **Figure 8a**) are superimposed at large strain values (illustration reproduced from **Figure 5b** but with a different scale for the y-axis to better reflect the evolution upon straining). This is even better illustrated in **Figure 8d** which is a zoomed-in view of **Figure 8a** at large normalized tensile strain. This suggests, as previously emphasized, that during the early stages of plastic deformation the most strained regions are mostly found in the CZ. Between YS and IP (**Figure 8b**,**e**), the FZ starts contributing substantially to the most strained regions. Beyond the IP, the most strained regions are now preferentially located in the FZ while the less deformed regions are located in the CZ, see **Figure 8c**,**f**. The tail of the distribution is now mostly associated with the deformation of the FZ (**Figure 8f**). The complete evolution of the strain distributions during plastic deformation can be found in **Video 6**.

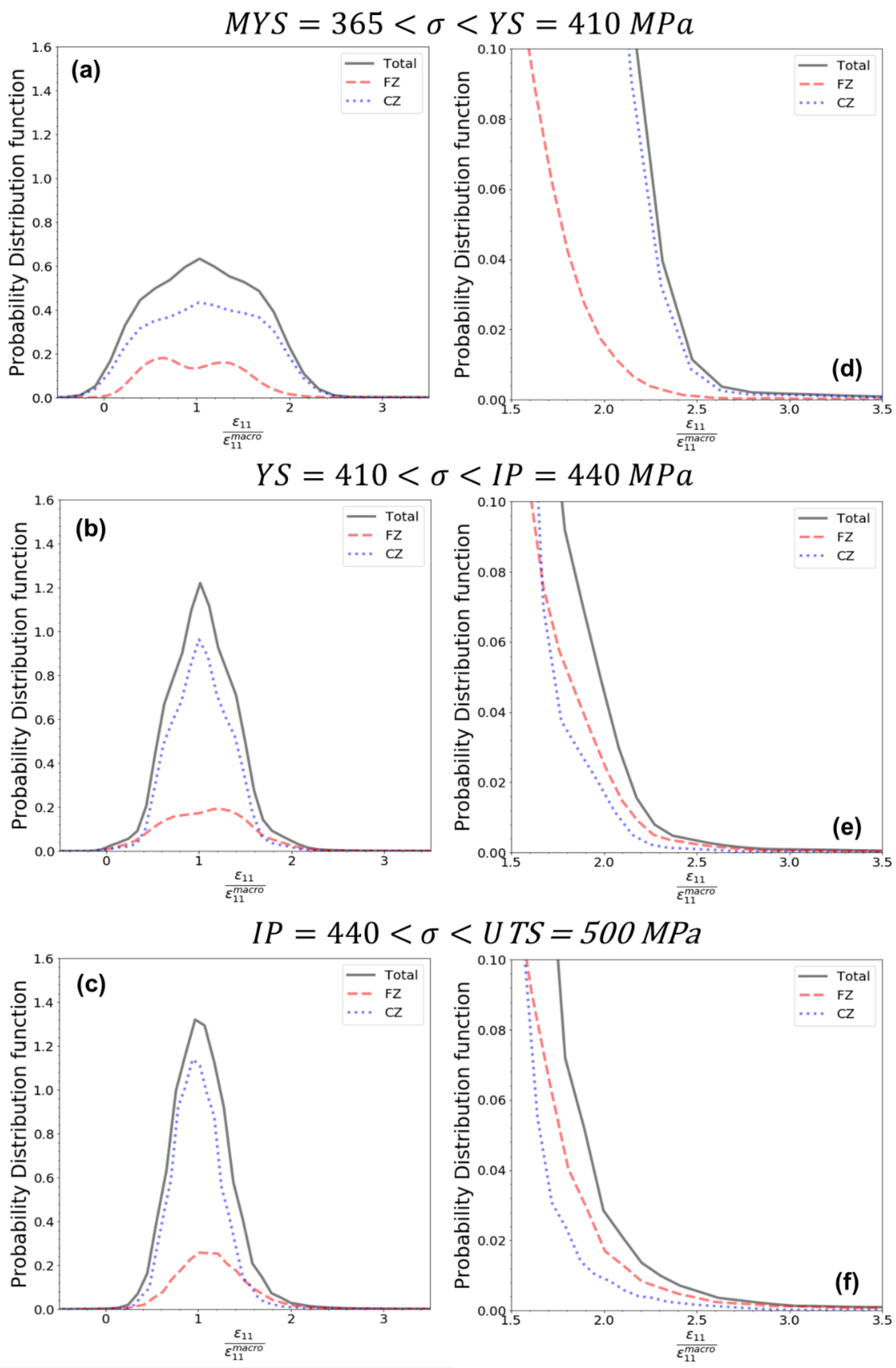

Figure 8. Evolution of the probability distribution functions of the local tensile strain in the FZ, CZ and entire ROI during tensile straining in the SR+400°C/1h sample along with zoom-in views of the tail of the strain distributions: (a,d) MYS < σ < YS; (b,e) YS < σ < IP; and (c,f) IP < σ < UTS.

To further investigate the evolution of the strain distribution during plastic deformation, we determined the respective proportion of FZ and CZ involved in the 5% most strained points in the whole ROI. Based on **Figure 9**, one can see how the 5% most strained regions are distributed between the FZ and CZ. During the early stages of plastic deformation, the 5% the most strained regions are predominantly found in the CZ. Nearly 75% of the 5% most strained regions are located in the CZ. When the macroscopic tensile strain approaches 0.02 (end of the stress plateau), the FZ and CZ contribute equally to the 5% most deformed regions. For stresses larger than the IP, the FZ is more involved in the 5% the most strained.

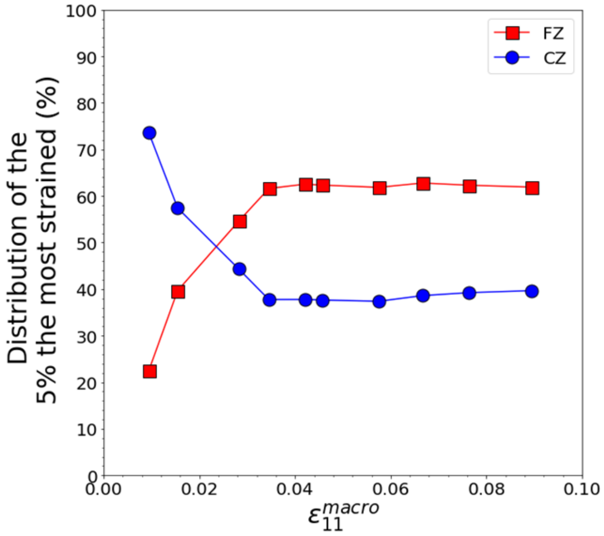

Figure 9. Evolution of the 5% the most deformed regions in the entire ROI as a function of the macroscopic tensile strain in the SR+400°C/1h sample.

3.5.3. Focus on the microscale strain distribution in the FZ

Focusing on the evolution of the local plastic strain in the FZ allows the observation of additional phenomena. Enlarged views of the region of interest highlighted using a white box in **Figure 7b**, **c**, **d**, and **f** are displayed in **Figure 10a-d**. Interestingly, plastic deformation seems to propagate in the FZ, this is particularly true between YS and IP (region associated with the stress plateau in the strain-strain response). The dashed black arrow in **Figure 10b** and **c** indicate the propagation of the plastic strain in the FZ. This phenomenon suggesting that the propagation of deformation bands seems to be restricted to the FZ.

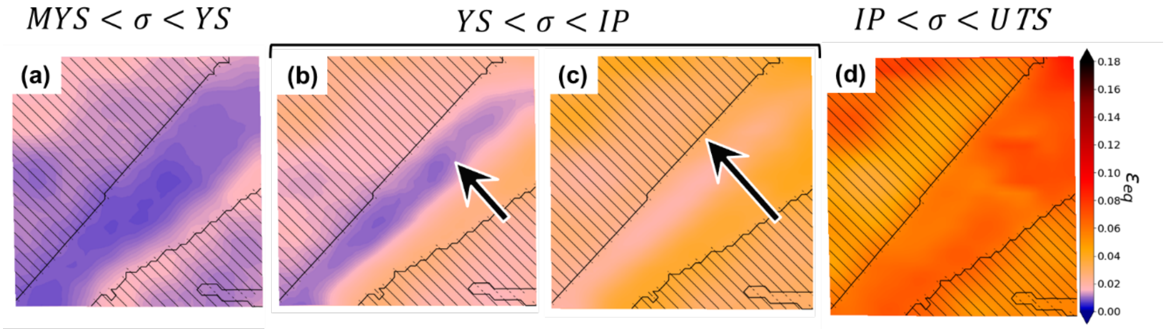

Figure 10. (a-d) Enlarged views of the region of interest highlighted using a white box in **Figure 7a-d** *for different levels of macroscopic tensile stress: (a) $MYS < \sigma < YS$; (b) $YS < \sigma < IP$; (c) $\sigma \geq IP$; $\sigma >> IP$. The black lines correspond to the interfaces between FZ and CZ. The CZ is identified as the hatched areas.*

A video of the successive deformation fields is provided in supplementary materials, see **Video 5**, and enables a better visualization of the evolutions described above.

For the sake of clarity, the demonstration here is based on the SR+400°C/1h sample but similar observations can be done when analyzing the microscale strain fields collected during in situ tensile testing of the SR (*Figure S 8a-d*) and SR+4h/400°C (*Figure S 9a-d*) samples. The videos corresponding to the evolution of the microscale strain fields of those two conditions are also provided as supplementary materials, see **Video 7** and **Video 8**. In those videos, the propagation of plastic deformation in the FZ can be seen at different locations. The only differences are the levels of stresses at which this phenomenon is observed. The case of the SR+400°C/96h sample differs slightly because the MYS cannot be identified, only the IP is clearly evidenced, see **Figure 3a-b**.

4. Discussion

4.1. On the origin of the micro-yield strength (MYS)

In the SR, SR+400°C/1h, and SR+400°C/4h samples, the MYS was clearly evidenced in **Figure 3b**. The onset of plastic deformation is observed in the CZ as well as near the MPBs. The MPBs consist mostly of FZ/CZ interfaces, i.e. those located at the bottom of the FZ (regions pointed with black arrows in **Figure 11**), but also of portions of FZ/FZ interfaces due to the percolation of the FZ (regions pointed with white arrows in **Figure 11**). Similar observations can be made in *Figure S 8a* and *Figure S 9a* for the SR and SR+400°C/4h samples respectively.

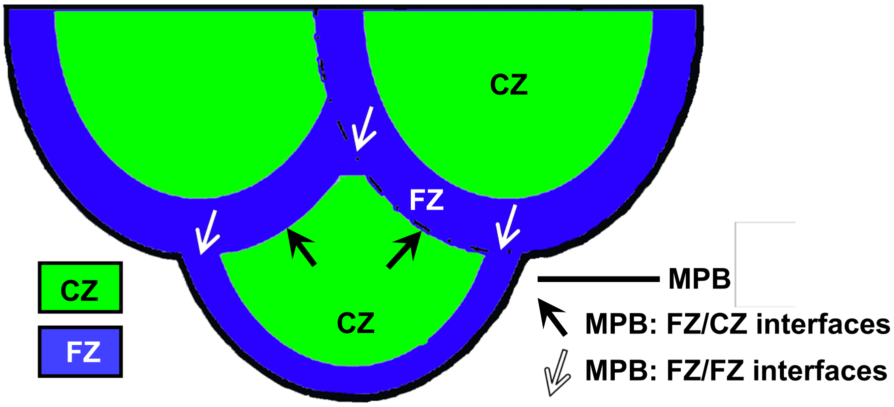

Figure 11. Schematic of the arrangement of the melt pools.

We will now discuss successively the reasons explaining why those two specific regions yield prior to the FZ.

To rationalize our observation that the CZ starts yielding before the FZ, the first objective was to obtain rough estimates of the respective yield strength (YS) of the FZ and CZ after a SR heat treatment as well as after ageing at 400°C/1h. The equations providing estimates of the different strengthening contributions in the FZ and CZ are given in **Appendix B**. We took into account grain boundary strengthening ($\Delta\sigma_{GB}$), solid solution strengthening ($\Delta\sigma_{SS}$), precipitation strengthening ($\Delta\sigma_{P}$) resulting from the formation of nanoscale L1$_2$-Al$_3$Zr precipitates upon ageing, and the composite effect through a load transfer mechanism ($\Delta\sigma_{LT}$) resulting from the presence of a significant proportion of intermetallic particles (about 20%). The contribution of the Mn-rich precipitates forming upon ageing at 400°C was ignored. Thus, one should be aware that we probably underestimate the YS in both FZ and CZ after ageing. All the constants used in the different equations are also summarized in **Table B. 1** given in **Appendix B**. The solid solution composition and the precipitate size and volume fraction were used to feed our strengthening models based on the results recently published in [36] and summarized in **Appendix B**. The estimates of the various sources of strengthening are provided in **Table 2**. The yield strength of the aluminium matrix in region *i* = FZ, CZ ($\sigma_{y,m}^{i}$) was taken as the sum of the different strengthening contributions using equation (1):

$$\sigma_{y,m}^{i} = \sigma_0 + \Delta\sigma_{GB}^{i} + \Delta\sigma_{SS}^{i} + \Delta\sigma_{P}^{i} \qquad (1)$$

The yield strength (YS^{i}) in the region *i* = FZ, CZ was then estimated using equation (2) based on a shear-lag model [47] assuming reinforcing particles with an aspect ratio of 1 to take into account the composite effect resulting from the load transfer from the aluminium matrix to the intermetallic particles ($\Delta\sigma_{S-L}^{i}$).

$$YS^i = \sigma_{y,m}^i + \Delta\sigma_{LT}^i \quad (2)$$

The increase in yield strength resulting from the intermetallic particles was estimated using equation (3).

$$\Delta\sigma_{LT}^i = \frac{1}{2} V_P^i \sigma_{y,m}^i \quad (3)$$

with V_P^i the volume fraction of intermetallic particles in the region i = FZ, CZ. Here, V_P^i = 0.20 regardless of the region considered FZ and CZ as previously done in our previous work dedicated to the same alloy [36].

		$\Delta\sigma_{GB}$ (MPa)	$\Delta\sigma_{SS}$ (MPa)	$\Delta\sigma_P$ (MPa)	$\sigma_{y,m}$ (MPa)	$\Delta\sigma_{S-L}$ (MPa)	**YS** (MPa)
SR	i = FZ	180	190	0	370	35	**405**
	i = CZ	50	210	0	260	25	**285**
SR + 400°C/1h	i = FZ	180	120	100	400	40	**440**
	i = CZ	50	125	140	315	30	**345**

Table 2 : Estimations of the various strengthening contributions in the FZ and CZ in the SR conditions and after ageing at 400°C/1h.

While the predictions of the values of the yield strength in the FZ and CZ should be considered carefully because many inputs are not necessarily properly measured or may suffer from a non-negligible degree of variability, the analysis of the results suggests that indeed the CZ yields before the FZ, especially due to a greater contribution of grain boundary strengthening in the FZ. Indeed, the results given in **Table 2** reveal that $YS^{FZ} - YS^{CZ} \approx 120$ MPa in the SR conditions, and $YS^{FZ} - YS^{CZ} \approx 95$ MPa after SR+400°C/1h. This relatively rough analysis suggests that the difference in YS between the FZ and CZ tends to be reduced after ageing at 400°C. After ageing, this difference is most likely much smaller because we did not take into account the strengthening effect of Mn-rich precipitates and those were observed in a larger proportion in the CZ in comparison with the FZ [36].

It is now necessary to discuss the specificity of the regions near the MPBs from a microstructural point of view. Those specific regions have with a specific thermal history because this is a region that can be partially remelted, heat affected, or subjected to different solidification conditions (lower solidification velocity). Several regions where plastic deformation initiates were examined carefully and no major microstructure change with respect to its immediate vicinity was clearly evidenced in the SEM images displayed in **Figure 6**. For example, no significant difference is found regarding the intermetallic particles which is consistent with the good thermal stability of the investigated material as discussed earlier in [36]. Those observations suggest that even if the regions near MPBs were thermally affected during the process, thermal variations would not be sufficient to induce microstructural evolutions that could be observed directly using SEM imaging. However, since areas close to MPBs are associated with regions where plastic deformation initiates upon straining, it suggests that those regions near MPBs are softer. The origin of such softer regions in the immediate vicinity of MPBs must be related to microstructural features at a finer scale (no local changes were evidenced using SEM). Our hypothesis is that in the as-fabricated conditions locally near the MPBs, the solid solution becomes slightly depleted in solutes, in particular, those retained in solid solution, here Mn and Zr [36]. Cu and Ni are mostly distributed in the intermetallics. This solid solution depletion in Mn and Zr would be related to different local solidification conditions (lower solidification velocity) or to a progression towards equilibrium of the intermetallics present at this location due to the larger time experienced at high temperatures. A slight solute variation in the as-built conditions could result in a locally reduced yield strength near the MPBs because a 0.1%.at decrease in Mn is expected to lead to a reduction in strength: $\Delta\sigma_{SS}^{Mn} = 12\ MPa\ /\ 0.1\ \%at\ Mn$ [48]. Here, the SR heat treatment is thought to be too short to suppress these local chemical heterogeneities through diffusion, see **Table 3** for the estimations of the diffusion distances for the two slow-diffusing elements. While Zr shows a much lower solid solution contribution to the strength ($\Delta\sigma_{SS}^{Zr} = 2\ MPa\ /\ 0.1\%at\ Zr$, after ageing at 400°C/1h a depletion in Zr may result in a lower density of nanoscale $L1_2$-Al_3Zr precipitates that would also contribute to a local decrease in strength. Interestingly, this heterogeneity at the atomic scale leading to a local decrease in strength near the MPBs seems to be lessened in the SR+400°C/4h and suppressed in the overaged sample (SR+400°C/96h). This can be explained by the difference in composition of the solid solution that becomes more homogeneous as it tends towards a thermodynamically driven equilibrium level, and by the coalescing precipitates that provide lower strengthening. Complementary investigations of the local composition of the solid solution in the SR conditions using site-specific lift-outs in the close vicinity of MPBs and APT measurements would be required to confirm our assumption.

	D_0 (m^2/s)	*Q* (kJ/Mol)	Ref	Diffusion lengths (nm)			
				SR (300°C/4h)	SR + 400°C/1h	SR + 400°C/4h	SR + 400°C/96h
Zr	0.0728	242	[49]	0.73	16.8	32.9	158.4
Mn	0.0135	211.5	[50]	7.8	113.6	219.3	1044.1

Table 3. Estimations of the diffusion lengths given in nm of the various solutes included in the Al-Mn-Ni-Cu-Zr alloy after the different heat treatments. The diffusion length was estimated using $L_i = (6D_it)^{0.5}$ *where t the time spent at T and* D_i *the diffusion coefficient calculated at the same T.*

To summarize, we propose that the origin of the MYS is correlated to (i) a lower YS in the CZ in comparison with the FZ due to differences in strengthening mechanisms, in particular grain boundary strengthening; and (ii) to a local depletion in Mn and possibly Zr in the solid solution near the MPBs causing a local reduction in YS in those specific regions. We suggest that this local solute depletion is due to the local variations of the thermal conditions near the MPBs.

4.2. On the origin of the stress plateau

Following the YS, a stress plateau with very low work hardening is observed on the stress-strain curves as shown in in **Figure 3a**, particularly in the SR+400°C/1h and SR+400°C/4h samples. In the SR sample, the stress plateau is not obvious in the stress-strain response. However, its signature can be evidenced in the work-hardening rate vs. true stress plot (**Figure 3b**). Hereafter, we discuss what can be the causes of such a stress plateau.

4.2.1. The role of solute-dislocation interactions

The formation and propagation of deformation bands has often been associated with the dislocation-locking mechanism (e.g. Lüders instability). This phenomenon was historically observed in Al alloys with a solid solution rich in alloying elements, the most famous example is that of Al-Mg alloys, see e.g. [51]–[53]. In this case, solutes such as Mg lock the dislocations, and higher stresses are needed to unlock the dislocations pinned by solute atoms. At a first sight, given that the solid solution is supersaturated in Mn and Zr in the SR conditions [36], one could conclude that the stress plateau can be the result of interactions between solutes such as Zr and Mn and the dislocations. However, two observations made in this work lead us to seriously question the idea of a mechanism based on the interactions between solutes and dislocations.

(i) First, no evidence of the propagation of deformation bands is found using macroscale DIC regardless of the samples studied. As shown using microscale DIC, the deformation bands propagate preferentially in the FZ and did not seem to go through the CZ although the solid solution was still enriched in Mn and Zr, especially in both the SR and SR+400°C/1h samples, see APT measurements reported in [36].

(ii) Secondly, the tensile response of the overaged sample (SR+400°C/96h) still shows the presence of a stress plateau near YS although the content of solutes retained in solute solution is likely very low given the diffusion lengths estimated in **Table 3**. By assuming that the content in solutes retained in solid solution is negligible after 96h at 400°C, the presence of a stress plateau in the overaged sample is not consistent with the hypothesis of solute-dislocation interactions.

4.2.2. The role of the submicron grains on the work-hardening

We first would like to note that the only microstructural feature that remains nearly unchanged upon ageing is the grain size [36]. The pioneering work of Kocks and Mecking [54] is relevant to discuss the origin of a plastic instability such as a stress plateau upon straining. The equations of the Kocks-Mecking model [54] are recalled hereafter:

$$\frac{\partial \rho}{\partial \varepsilon} = \left[k_1\sqrt{\rho} - k_2\rho\right] \qquad (4)$$

$$\Delta\sigma_{DIS} = M\alpha G b\sqrt{\rho_{DIS}} \qquad (5)$$

where ρ is the dislocation density, ε is the plastic strain, and k_1 and k_2 are constants. Equation (4) reveals a positive contribution to the work-hardening ($k_1\sqrt{\rho}$) and a negative one ($k_2\rho$). The first term corresponds to dislocation production while the second term is associated with recovery (annihilation of dislocations of opposite sign). When those two terms become equal, the work hardening is equal to zero, a condition required to observe a stress plateau on a stress-strain response.

The literature dealing with the mechanical response of fine-grained Al alloys is particularly relevant to discuss the results obtained in this work [55]–[59]. Tsuji *et al.* [55] studied the mechanical behaviour of a 1100-commercial purity aluminium with grain sizes ranging from 270nm to 10µm. They showed that for grain sizes < 1µm, the yield strength was greatly improved but this goes along with a yield drop phenomenon followed by strain softening resulting in a loss of uniform elongation. Yu *et al.* [56] found similar results studying the tensile response of ultrafine-grained 1050 commercially pure Al. In microstructures consisting of submicron grains, the dislocations cannot be stored within grains and arranged in a sub-structure as classically observed in microstructures consisting of larger grains. Thus, in presence of submicron grains, the combination of a limited forest hardening contribution (limited dislocation storage) and an enhanced recovery contribution (grain boundaries can be considered as dislocation sinks) leads to a poor work-hardening capacity. In other words, when a mobile dislocation is created in a submicron grain, it shears the grain (no obstacle) before being stored at the grain boundaries. Since the grain size is below a critical value L_c also called the dislocation slip distance, there is no possibility for dislocations to be stored within the grain. This mechanism explains why the formation of dislocation cells is very difficult in submicron grains. Interestingly, Lloyd *et al.* [58] reported inhomogeneous yielding in a fine-grained Al-6Ni alloy and established a link with the propagation of deformation bands.

The recent study of Bayoumy *et al.* [27] is also an interesting piece of work to further discuss the present results. Micro tensile specimens were prepared using FIB and extracted from different regions in an Al-Mn-Sc alloy designed for L-PBF and showing a bimodal grain structure. The fine-grained region shows a significantly different tensile response in comparison with the coarse-grained region. The fine-grained region was found to have a higher yield strength (> 50 MPa) and interestingly showed a yield drop phenomenon followed by a strain softening stage. On the opposite, no yield drop was detected in the tensile response of the coarse-grained region, and a discernible work-hardening was observed. Bayoumy *et al.* [27] concluded that the stress plateau in the Al-Mn-Sc alloy was mainly caused by the fine-grained regions.

4.2.3. Application to our heterogeneous microstructure

As discussed above, there is strong evidence that a submicron grain size results in an absence of work hardening following the yield point. We can relate this feature to the evolution of microscopic deformation following the YS, and particularly the progressive propagation of plastic strain within the FZ in between the YS and the IP, which strengthens the hypothesis that the stress plateau is related to the small grain size of the FZ.

To further consolidate this analysis, we aimed to produce samples with the same powder batch (no composition changes) while inducing limited microstructural changes except an increase in the proportion of fine equiaxed grains. The stress plateau is thus expected to be more pronounced in the presence of a larger fraction of FZs assuming that the work-hardening capacity of the CZs is not altered. Increasing the preheating temperature from 35 et 200°C was found to be an efficient strategy to increase the volume fraction of fine equiaxed grains, see [60], [61]. Additional samples were thus fabricated using a build platform at 200°C instead of 100°C while keeping the other processing parameters constant. **Figure 12a** shows an example of such a sample subjected to SR+400°C/1h. This increase in the build platform temperature does not result in major microstructural changes regarding the intermetallic population (nature, size, and morphology). In addition, 200°C is not high enough to significantly alter the supersaturation in slow diffusing species such as Zr and Mn. Thus, the only important microstructural modification seems to occur at the grain scale with a higher area fraction of FZs. It was indeed found to be increased to 45 ± 5% (an increase of nearly 30% in comparison with the samples fabricated with a build platform at 100°C). Note that the same methodology as used in section 3.1. was employed to estimate the area fraction of FZs. The tensile response of this new sample is given in **Figure 12b**. It is rather clear that the stress plateau is larger in comparison to what can be observed in samples fabricated with a build substrate hold at 100°C.

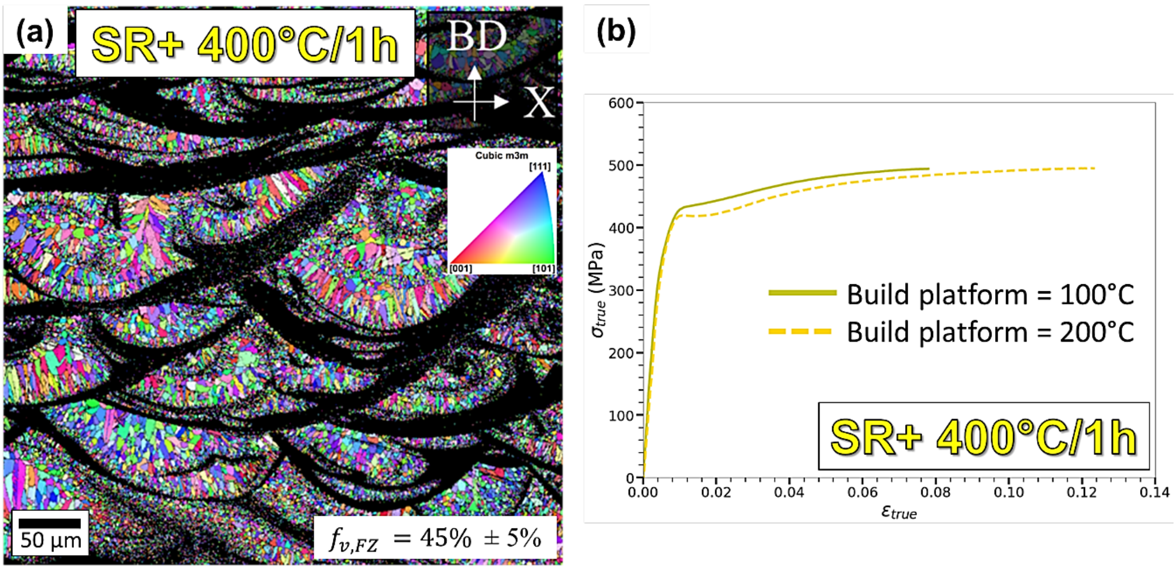

Figure 12. (a) EBSD-IPF map of aluminium revealing the bimodal grain structure with a larger fraction of fine equiaxed zones (FZ, mostly in black), about 45%, due to the increase of the build platform temperature from 100°C to 200°C. (b) Tensile response of the sample fabricated with a build platform at 200°C and subjected to SR+400°C/1h. The tensile response of the same conditions but with a build platform at 100°C is given for comparison.

Finally, an in situ tensile test in the SEM was conducted with this new sample fabricated with a build platform at 200°C, see the strain fields in **Figure 13a-f**. Here, to better illustrate the propagation of plastic deformation in the FZ, 4 successive strain fields taken between YS and IP are shown, see **Figure 13b-e**. The reader is also invited to look at **Video 9** for the successive strain maps acquired during tensile straining and **Video 10** for the evolution of the strain distributions upon straining. Probability distribution functions in the entire ROI as well as in the FZ and CZ respectively are also provided in supplementary materials, see *Figure S 11*. The propagation of deformation bands in the FZ is nicely evidenced, see the area highlighted in white in **Figure 13**. The arrow indicates the direction of the propagation of plastic deformation. Those observations confirm the previous results shown in **Figure 10a-d**.

It thus appears reasonable to conclude that the stress plateau evidenced in this work is caused by the presence of submicron grains. The interconnection of the FZs in 3D helps to understand why the stress plateau can be seen directly on the macroscopic tensile response although the fraction of fine equiaxed grains represents only about 35% of the microstructure at the grain scale.

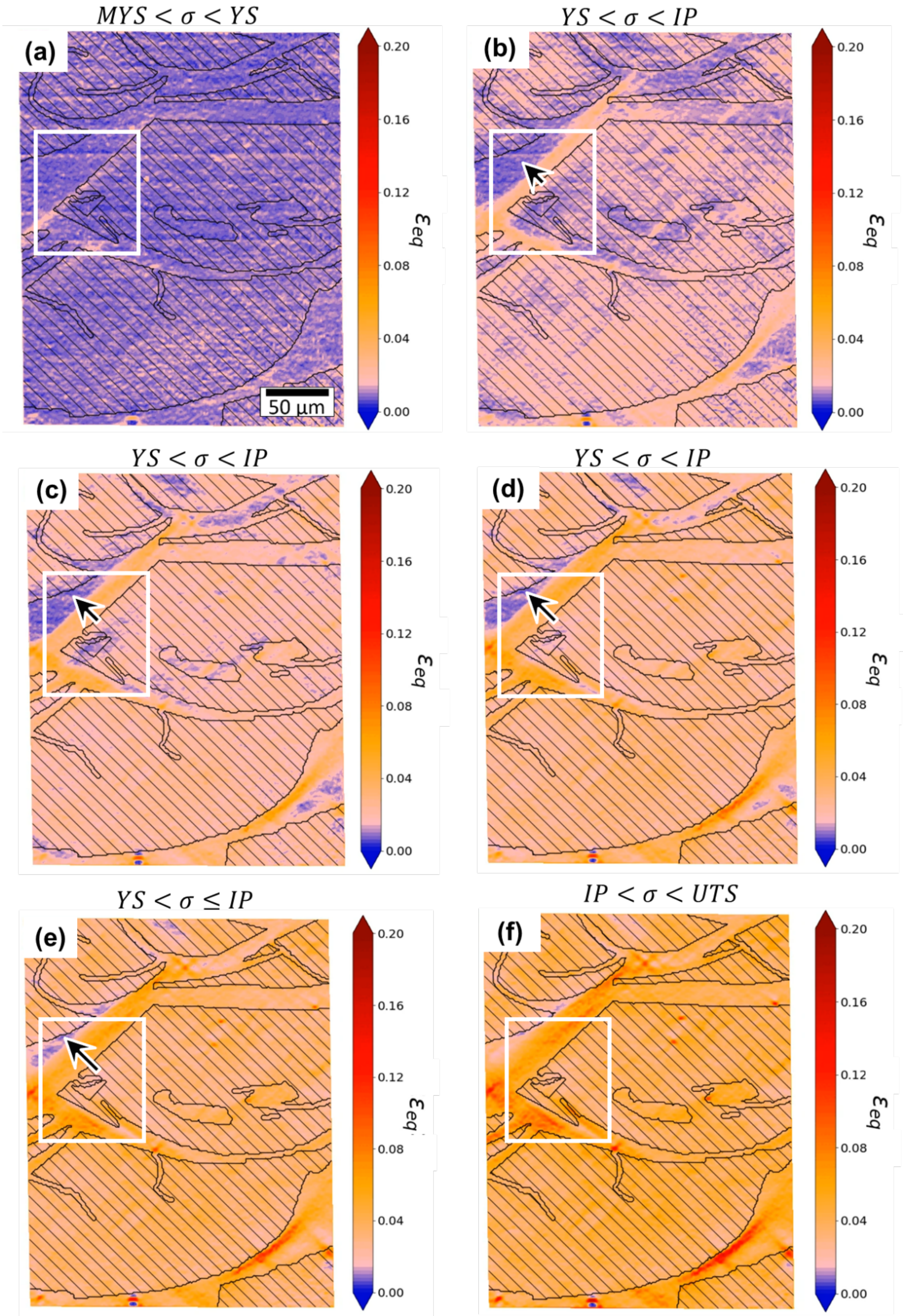

Figure 13. (a-f) Microscale strain fields determined in the SR+400°C/1h sample (build temperature 200°C) using DIC for different levels of macroscopic tensile stress: (a) MYS < σ < YS; (b-e) YS < σ < IP; (f); IP < σ < UTS. The black lines correspond to the interfaces between FZ and CZ. The CZ is identified as the hatched areas.

4.3. Guidelines to tailor the tensile response of Al alloys designed for L-PBF

Interestingly, we found a lot of publications dedicated to new Al alloys designed for L-PBF and having a bimodal grain structure where the tensile response shows a stress plateau with the presence of a yield drop phenomenon or a strain softening stage, see e.g. [5], [11]–[13], [15]–[17], [27], [62]. However, very few studies have attempted to clarify the tensile response in light of the heterogeneous nature of the microstructure [27]. Thus, we believe that the results presented in this work can be helpful to clarify the tensile responses of many Al alloys designed for L-PBF and showing a heterogeneous grain structure with the presence of a significant proportion of submicron grains.

A schematic illustration of the tensile response of the bimodal grain structure is proposed in **Figure 14** (black curve) along with the typical mechanical behaviour of the FZ (in red) and CZ (in blue). The FZ shows a higher yield strength but poor work-hardening in comparison with the CZ in agreement with the recent results of Bayoumy *et al.* [27]. Note that here microyielding was associated with the CZ but also with the regions in the close vicinity of MPBs that can be considered as soft regions.

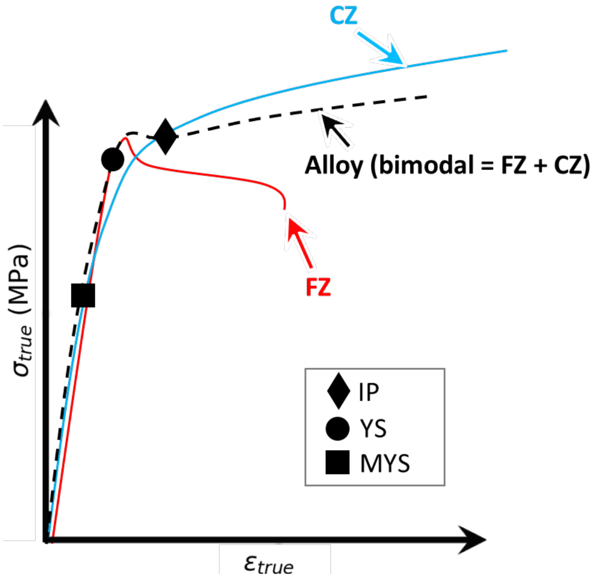

Figure 14. Schematic illustration of the tensile response of a bimodal microstructure (in black) consisting of a significant proportion of submicron grains (FZ) and coarser grain (> 5 µm). The typical tensile response of the FZ and CZ is also given in red and blue respectively.

In the presence of a microstructure full of equiaxed grains with a size typically < 1µm, one would expect no work-hardening capacity and a material very sensitive to strain localization (red curve in **Figure 14**). On the opposite, a coarse-grained microstructure is expected to work harden (blue curve in **Figure 14**). Considering now a composite material with fine-grained and coarse-grained regions, the tensile response shows characteristics of both microstructures. Here, the yield strength of the CZs needs to be lower than that of the FZs, otherwise, one would observe catastrophic failure due to early strain localization in the FZ, especially considering the 3D interconnection of the FZs (**Figure 2d**). It is also believed that the CZ contributes to delay strain localization in the FZ due to the topology of the microstructure. The main source of the work-hardening capacity of the composite material is thus mostly attributed to the CZs even though more work is needed to investigate the amplitude of the back-stress caused by the intermetallic particles that could bring a kinematic contribution to the work-hardening.

The outcomes from this work can provide guidelines to tailor the mechanical response of Al alloys designed for LPBF. Different strategies can be suggested to tune the relative proportion of FZs and CZs as well as their spatial distribution. Manipulating the processing parameters was already proven to affect the fraction of FZ [60], [61] and was confirmed in the present study. One can also consider adjusting the content of solutes involved in the precipitation of the primary $L1_2$-Al_3X phase to control the proportion of FZ. Finally, tuning the relative strength of the FZ and CZ also appears as an interesting pathway to tailor the overall mechanical response.

5. Conclusion

This work brings new insights into the tensile mechanical behaviour of Al alloys designed for L-PBF and showing a bimodal grain structure with the presence of a relatively large proportion of submicron grains (>20%) distributed along the MPBs and interconnected in 3D as revealed here using synchrotron nano-CT and machine learning-assisted segmentation.

The elastoplastic transition is characterized by micro-yielding and the presence of a stress plateau following the YS. Those characteristics can be observed directly in the stress-strain response regardless of the heat treatment but are better highlighted using the logarithmic derivative reflecting variations in work-hardening rate. Although the tensile responses show the presence of a peculiar elastoplastic transition, no insights could be gained from macroscale DIC suggesting that the underlying phenomena take place at a finer scale. Thus, micron-scale DIC measurements were carried out.

The following insights were gained from microscale DIC:

- Softer regions in the CZ and near the MPBs are thus thought to be responsible for the MYS for all conditions except the SR+400°C/96h sample for which no distinction can be made between MYS and YS. The CZ yields prior to the FZ due to a greater contribution of grain boundary strengthening in the FZ. The specific thermal history of the MPBs can be invoked to account for their specific behaviour. Our hypothesis is that there is a local redistribution of solutes near the MPBs which leads to a locally depleted solid solution resulting in softer regions. Further local atomic characterization is required to confirm this assumption.
- Between YS and IP, a stress plateau is observed and the mechanical response is dominated by the FZs in which the propagation of deformation bands is observed.
- Beyond the IP, once deformation bands have swept the FZs, strain starts localizing in the FZs.

The stress plateau is caused by the presence of submicron grains showing a poor work-hardening capacity. The work-hardening capacity of the investigated material is attributed to the CZs. It is concluded that optimizing the respective proportion of FZs and CZs, their 3D spatial distribution as well as their relative strength can be an interesting pathway to tailor the tensile response of Al alloys designed for L-PBF.

Acknowledgements

The authors are grateful to the AEROPRINT project supported by the Région Rhône-Alpes Auvergne. This work has benefited from the characterization equipment of the Grenoble INP CMTC platform supported by the Centre of Excellence of Multifunctional Architectured Materials "CEMAM" n◦ANR-10-LABX-44-01 funded by the Investments for the Future program. The European Synchrotron Radiation Facility (ESRF) is gratefully acknowledged for offering beamtime at ID16B associated with proposals MA4632, MA5086, and MA4928.

References

[1] G. Del Guercio *et al.*, « Cracking behaviour of high-strength AA2024 aluminium alloy produced by Laser Powder Bed Fusion », *Additive Manufacturing*, vol. 54, p. 102776, juin 2022, doi: 10.1016/j.addma.2022.102776.

[2] S. Z. Uddin, L. E. Murr, C. A. Terrazas, P. Morton, D. A. Roberson, et R. B. Wicker, « Processing and characterization of crack-free aluminum 6061 using high-temperature heating in laser powder bed fusion additive manufacturing », *Additive Manufacturing*, vol. 22, p. 405-415, août 2018, doi: 10.1016/j.addma.2018.05.047.

[3] A. Sonawane, G. Roux, J.-J. Blandin, A. Despres, et G. Martin, « Cracking mechanism and its sensitivity to processing conditions during laser powder bed fusion of a structural aluminum alloy », *Materialia*, vol. 15, p. 100976, mars 2021, doi: 10.1016/j.mtla.2020.100976.

[4] W. Stopyra, K. Gruber, I. Smolina, T. Kurzynowski, et B. Kuźnicka, « Laser powder bed fusion of AA7075 alloy: Influence of process parameters on porosity and hot cracking », *Additive Manufacturing*, vol. 35, p. 101270, oct. 2020, doi: 10.1016/j.addma.2020.101270.

[5] J. H. Martin, B. D. Yahata, J. M. Hundley, J. A. Mayer, T. A. Schaedler, et T. M. Pollock, « 3D printing of high-strength aluminium alloys », *Nature*, vol. 549, n° 7672, p. 365-369, sept. 2017, doi: 10.1038/nature23894.

[6] P. Mair, L. Kaserer, J. Braun, N. Weinberger, I. Letofsky-Papst, et G. Leichtfried, « Microstructure and mechanical properties of a TiB2-modified Al–Cu alloy processed by laser powder-bed fusion », *Materials Science and Engineering: A*, vol. 799, p. 140209, janv. 2021, doi: 10.1016/j.msea.2020.140209.

[7] S. Ma *et al.*, « Additive manufacturing enabled synergetic strengthening of bimodal reinforcing particles for aluminum matrix composites », *Additive Manufacturing*, vol. 70, p. 103543, mai 2023, doi: 10.1016/j.addma.2023.103543.

[8] P. Mair *et al.*, « Laser powder bed fusion of nano-CaB6 decorated 2024 aluminum alloy », *Journal of Alloys and Compounds*, vol. 863, p. 158714, mai 2021, doi: 10.1016/j.jallcom.2021.158714.

[9] J. R. Croteau *et al.*, « Microstructure and mechanical properties of Al-Mg-Zr alloys processed by selective laser melting », *Acta Materialia*, vol. 153, p. 35-44, juill. 2018, doi: 10.1016/j.actamat.2018.04.053.

[10] S. Griffiths, M. D. Rossell, J. Croteau, N. Q. Vo, D. C. Dunand, et C. Leinenbach, « Effect of laser rescanning on the grain microstructure of a selective laser melted Al-Mg-Zr alloy », *Materials Characterization*, vol. 143, p. 34-42, sept. 2018, doi: 10.1016/j.matchar.2018.03.033.

[11] M. Genc *et al.*, « Optimization of the strength vs. conductivity trade-off in an aluminium alloy designed for laser powder bed fusion », *Materials Science and Engineering: A*, vol. 858, p. 144139, nov. 2022, doi: 10.1016/j.msea.2022.144139.

[12] Q. Li *et al.*, « Development of a high strength Zr/Sc/Hf-modified Al-Mn-Mg alloy using Laser Powder Bed Fusion: Design of a heterogeneous microstructure incorporating synergistic multiple strengthening mechanisms », *Additive Manufacturing*, vol. 57, p. 102967, sept. 2022, doi: 10.1016/j.addma.2022.102967.

[13] A. Mehta *et al.*, « Additive manufacturing and mechanical properties of the dense and crack free Zr-modified aluminum alloy 6061 fabricated by the laser-powder bed fusion », *Additive Manufacturing*, vol. 41, p. 101966, mai 2021, doi: 10.1016/j.addma.2021.101966.

[14] M. Opprecht, J.-P. Garandet, G. Roux, C. Flament, et M. Soulier, « A solution to the hot cracking problem for aluminium alloys manufactured by laser beam melting », *Acta Materialia*, vol. 197, p. 40-53, sept. 2020, doi: 10.1016/j.actamat.2020.07.015.

[15] Q. Jia *et al.*, « Selective laser melting of a high strength Al Mn Sc alloy: Alloy design and strengthening mechanisms », *Acta Materialia*, vol. 171, p. 108-118, juin 2019, doi: 10.1016/j.actamat.2019.04.014.

[16] Q. Jia *et al.*, « Precipitation kinetics, microstructure evolution and mechanical behavior of a developed Al–Mn–Sc alloy fabricated by selective laser melting », *Acta Materialia*, vol. 193, p. 239-251, juill. 2020, doi: 10.1016/j.actamat.2020.04.015.

[17] J. Lu *et al.*, « On the Sc induced solidification-heterogeneous microstructure in selective laser melted Al-5Mn alloys », *Journal of Materials Processing Technology*, vol. 304, p. 117562, juin 2022, doi: 10.1016/j.jmatprotec.2022.117562.

[18] F. Leijon, S. Wachter, Z. Fu, C. Körner, S. Skjervold, et J. Moverare, « A novel rapid alloy development method towards powder bed additive manufacturing, demonstrated for binary Al-Ti, -Zr and -Nb alloys », *Materials & Design*, vol. 211, p. 110129, déc. 2021, doi: 10.1016/j.matdes.2021.110129.

[19] M. Roscher, S. Balachandran, D. Mayweg, et E. Jägle, « Development of Al-Ti-based alloys for laser powder bed fusion », *Additive Manufacturing*, vol. 47, p. 102315, nov. 2021, doi: 10.1016/j.addma.2021.102315.

[20] F. Xiao *et al.*, « Niobium nanoparticle-enabled grain refinement of a crack-free high strength Al-Zn-Mg-Cu alloy manufactured by selective laser melting », *Journal of Alloys and Compounds*, vol. 900, p. 163427, avr. 2022, doi: 10.1016/j.jallcom.2021.163427.

[21] Z. Wang, X. Wang, X. Chen, et C. Qiu, « Complete columnar-to-equiaxed transition and significant grain refinement in an aluminium alloy by adding Nb particles through laser powder bed fusion », *Additive Manufacturing*, vol. 51, p. 102615, mars 2022, doi: 10.1016/j.addma.2022.102615.

[22] J. H. Martin *et al.*, « Grain refinement mechanisms in additively manufactured nano-functionalized aluminum », *Acta Materialia*, vol. 200, p. 1022-1037, nov. 2020, doi: 10.1016/j.actamat.2020.09.043.

[23] M. Schuster, A. De Luca, A. Mathur, E. Hosseini, et C. Leinenbach, « Precipitation in a 2xxx series Al-Cu-Mg-Zr alloy fabricated by laser powder bed fusion », *Materials & Design*, vol. 211, p. 110131, déc. 2021, doi: 10.1016/j.matdes.2021.110131.

[24] C. Pauzon, M. Buttard, A. Després, B. Chehab, J.-J. Blandin, et G. Martin, « A novel laser powder bed fusion Al-Fe-Zr alloy for superior strength-conductivity trade-off », *Scripta Materialia*, vol. 219, p. 114878, oct. 2022, doi: 10.1016/j.scriptamat.2022.114878.

[25] M. Buttard *et al.*, « Multi-scale microstuctural investigation of a new Al-Mn-Ni-Cu-Zr aluminium alloy processed by laser powder bed fusion », *Materialia*, vol. 18, p. 101160, août 2021, doi: 10.1016/j.mtla.2021.101160.

[26] C. Pauzon *et al.*, « Direct ageing of LPBF Al-1Fe-1Zr for high conductivity and mechanical performance », *Acta Materialia*, vol. 258, p. 119199, oct. 2023, doi: 10.1016/j.actamat.2023.119199.

[27] D. Bayoumy *et al.*, « Origin of non-uniform plasticity in a high-strength Al-Mn-Sc based alloy produced by laser powder bed fusion », *Journal of Materials Science & Technology*, vol. 103, p. 121-133, mars 2022, doi: 10.1016/j.jmst.2021.06.042.

[28] M. Opprecht, J.-P. Garandet, G. Roux, et C. Flament, « An understanding of duplex microstructures encountered during high strength aluminium alloy laser beam melting processing », *Acta Materialia*, vol. 215, p. 117024, août 2021, doi: 10.1016/j.actamat.2021.117024.

[29] W. Lefebvre, G. Rose, P. Delroisse, E. Baustert, F. Cuvilly, et A. Simar, « Nanoscale periodic gradients generated by laser powder bed fusion of an AlSi10Mg alloy », *Materials & Design*, vol. 197, p. 109264, janv. 2021, doi: 10.1016/j.matdes.2020.109264.

[30] Y. Otani, N. Takata, A. Suzuki, M. Kobashi, et M. Kato, « Microstructural origin of anisotropic tensile ductility of Al-Si alloy manufactured by laser powder bed fusion », *Scripta Materialia*, vol. 226, p. 115259, mars 2023, doi: 10.1016/j.scriptamat.2022.115259.

[31] J. Fite, S. E. Prameela, J. Slotwinski, et T. P. Weihs, « Melt pool boundaries in additively manufactured AlSi10Mg: Correlating inhomogeneous deformation with local microstructure via in-situ microtensile tests », *Materials Science and Engineering: A*, vol. 882, p. 145431, août 2023, doi: 10.1016/j.msea.2023.145431.

[32] T. Ajantiwalay, R. Michi, C. Roach, A. Shyam, A. Plotkowski, et A. Devaraj, « Influence of microstructural heterogeneities on small-scale mechanical properties of an additively manufactured Al-Ce-Ni-Mn alloy », *Additive Manufacturing Letters*, vol. 3, p. 100092, déc. 2022, doi: 10.1016/j.addlet.2022.100092.

[33] R. S. Haridas *et al.*, « Synergy of tensile strength and high cycle fatigue properties in a novel additively manufactured Al-Ni-Ti-Zr alloy with a heterogeneous microstructure », *Additive Manufacturing*, vol. 62, p. 103380, janv. 2023, doi: 10.1016/j.addma.2022.103380.

[34] A. Dhal, S. Thapliyal, S. Gaddam, P. Agrawal, et R. S. Mishra, « Multiscale hierarchical and heterogeneous mechanical response of additively manufactured novel Al alloy investigated by high-resolution nanoindentation mapping », *Sci Rep*, vol. 12, n° 1, p. 18344, oct. 2022, doi: 10.1038/s41598-022-23083-2.

[35] M. Buttard *et al.*, « Towards an alloy design strategy by tuning liquid local ordering: What solidification of an Al-alloy designed for laser powder bed fusion teaches us », *Additive Manufacturing*, vol. 61, p. 103313, janv. 2023, doi: 10.1016/j.addma.2022.103313.

[36] M. Buttard *et al.*, « Ageing response and strengthening mechanisms in a new Al-Mn-Ni-Cu-Zr alloy designed for laser powder bed fusion », *Acta Materialia*, vol. 259, p. 119271, oct. 2023, doi: 10.1016/j.actamat.2023.119271.

[37] P. Cloetens *et al.*, « Holotomography: Quantitative phase tomography with micrometer resolution using hard synchrotron radiation x rays », *Applied Physics Letters*, vol. 75, n° 19, p. 2912-2914, nov. 1999, doi: 10.1063/1.125225.

[38] A. Mirone, E. Brun, E. Gouillart, P. Tafforeau, et J. Kieffer, « The PyHST2 hybrid distributed code for high speed tomographic reconstruction with iterative reconstruction and a priori knowledge capabilities », *Nuclear Instruments and Methods in Physics Research Section B: Beam Interactions with Materials and Atoms*, vol. 324, p. 41-48, avr. 2014, doi: 10.1016/j.nimb.2013.09.030.

[39] L. Allais, M. Bornert, T. Bretheau, et D. Caldemaison, « Experimental characterization of the local strain field in a heterogeneous elastoplastic material », *Acta Metallurgica et Materialia*, vol. 42, n° 11, p. 3865-3880, nov. 1994, doi: 10.1016/0956-7151(94)90452-9.

[40] E. Héripré *et al.*, « Coupling between experimental measurements and polycrystal finite element calculations for micromechanical study of metallic materials », *International*

Journal of Plasticity, vol. 23, nº 9, p. 1512-1539, sept. 2007, doi: 10.1016/j.ijplas.2007.01.009.

[41] G. Martin *et al.*, « A macro- and micromechanics investigation of hot cracking in duplex steels », *Acta Materialia*, vol. 60, nº 11, p. 4646-4660, juin 2012, doi: 10.1016/j.actamat.2012.03.040.

[42] M. Rappaz, Ph. Jarry, G. Kurtuldu, et J. Zollinger, « Solidification of Metallic Alloys: Does the Structure of the Liquid Matter? », *Metall Mater Trans A*, vol. 51, nº 6, p. 2651-2664, juin 2020, doi: 10.1007/s11661-020-05770-9.

[43] M. A. Salgado-Ordorica, A. B. Phillion, et M. Rappaz, « Morphology and Growth Kinetic Advantage of Quenched Twinned Dendrites in Al-Zn Alloys », *Metall Mater Trans A*, vol. 44, nº 6, p. 2699-2706, juin 2013, doi: 10.1007/s11661-012-1539-0.

[44] M. A. Salgado-Ordorica et M. Rappaz, « Twinned dendrite growth in binary aluminum alloys », *Acta Materialia*, vol. 56, nº 19, p. 5708-5718, nov. 2008, doi: 10.1016/j.actamat.2008.07.046.

[45] Y. Li, S. Li, L. Yang, et H. Zhong, « Microstructure and properties of twinned dendrites in directionally solidified A356 alloy », *Materials Science and Engineering: A*, vol. 734, p. 7-19, sept. 2018, doi: 10.1016/j.msea.2018.07.079.

[46] V. Samaee, M. Dupraz, T. Pardoen, H. Van Swygenhoven, D. Schryvers, et H. Idrissi, « Deciphering the interactions between single arm dislocation sources and coherent twin boundary in nickel bi-crystal », *Nat Commun*, vol. 12, nº 1, p. 962, févr. 2021, doi: 10.1038/s41467-021-21296-z.

[47] V. C. Nardone et K. M. Prewo, « On the strength of discontinuous silicon carbide reinforced aluminum composites », *Scripta Metallurgica*, vol. 20, nº 1, p. 43-48, janv. 1986, doi: 10.1016/0036-9748(86)90210-3.

[48] T. Uesugi et K. Higashi, « First-principles studies on lattice constants and local lattice distortions in solid solution aluminum alloys », *Computational Materials Science*, vol. 67, p. 1-10, févr. 2013, doi: 10.1016/j.commatsci.2012.08.037.

[49] Y. Du *et al.*, « Diffusion coefficients of some solutes in fcc and liquid Al: critical evaluation and correlation », *Materials Science and Engineering: A*, vol. 363, nº 1-2, p. 140-151, déc. 2003, doi: 10.1016/S0921-5093(03)00624-5.

[50] K. E. Knipling, D. C. Dunand, et D. N. Seidman, « Criteria for developing castable, creep-resistant aluminum-based alloys – A review », *MEKU*, vol. 97, nº 3, p. 246-265, mars 2006, doi: 10.3139/146.101249.

[51] J. G. Morris, « Lüders bands in Al—Mg alloys », *Materials Science and Engineering*, vol. 5, nº 5, p. 299-302, mai 1970, doi: 10.1016/0025-5416(70)90021-2.

[52] J. Coër, P. Y. Manach, H. Laurent, M. C. Oliveira, et L. F. Menezes, « Piobert–Lüders plateau and Portevin–Le Chatelier effect in an Al–Mg alloy in simple shear », *Mechanics Research Communications*, vol. 48, p. 1-7, mars 2013, doi: 10.1016/j.mechrescom.2012.11.008.

[53] R. N. De Codes, O. S. Hopperstad, O. Engler, O.-G. Lademo, J. D. Embury, et A. Benallal, « Spatial and Temporal Characteristics of Propagating Deformation Bands in AA5182 Alloy at Room Temperature », *Metall Mater Trans A*, vol. 42, nº 11, p. 3358-3369, nov. 2011, doi: 10.1007/s11661-011-0749-1.

[54] U. F. Kocks et H. Mecking, « Physics and phenomenology of strain hardening: the FCC case », *Progress in Materials Science*, vol. 48, nº 3, p. 171-273, janv. 2003, doi: 10.1016/S0079-6425(02)00003-8.

[55] N. Tsuji, Y. Ito, Y. Saito, et Y. Minamino, « Strength and ductility of ultrafine grained aluminum and iron produced by ARB and annealing », *Scripta Materialia*, vol. 47, nº 12, p. 893-899, déc. 2002, doi: 10.1016/S1359-6462(02)00282-8.

[56] C. Y. Yu, P. W. Kao, et C. P. Chang, « Transition of tensile deformation behaviors in ultrafine-grained aluminum », *Acta Materialia*, vol. 53, nº 15, p. 4019-4028, sept. 2005, doi: 10.1016/j.actamat.2005.05.005.

[57] P. Hung, P. Sun, C. Yu, P. Kao, et C. Chang, « Inhomogeneous tensile deformation in ultrafine-grained aluminum », *Scripta Materialia*, vol. 53, nº 6, p. 647-652, sept. 2005, doi: 10.1016/j.scriptamat.2005.05.036.

[58] D. J. Lloyd et L. R. Morris, « Luders band deformation in a fine grained aluminium alloy », *Acta Metallurgica*, vol. 25, nº 8, p. 857-861, août 1977, doi: 10.1016/0001-6160(77)90170-5.

[59] D. J. Lloyd et H. Jin, « Inhomogeneous yielding and work hardening of a fine grained Al–Mg alloy », *Materials Science and Engineering: A*, vol. 585, p. 455-459, nov. 2013, doi: 10.1016/j.msea.2013.07.044.

[60] K. V. Yang, Y. Shi, F. Palm, X. Wu, et P. Rometsch, « Columnar to equiaxed transition in Al-Mg(-Sc)-Zr alloys produced by selective laser melting », *Scripta Materialia*, vol. 145, p. 113-117, mars 2018, doi: 10.1016/j.scriptamat.2017.10.021.

[61] Y. Shi, K. Yang, S. K. Kairy, F. Palm, X. Wu, et P. A. Rometsch, « Effect of platform temperature on the porosity, microstructure and mechanical properties of an Al–Mg–Sc–Zr alloy fabricated by selective laser melting », *Materials Science and Engineering: A*, vol. 732, p. 41-52, août 2018, doi: 10.1016/j.msea.2018.06.049.

[62] Z. Zhu *et al.*, « Superior mechanical properties of a selective-laser-melted AlZnMgCuScZr alloy enabled by a tunable hierarchical microstructure and dual-nanoprecipitation », *Materials Today*, vol. 52, p. 90-101, janv. 2022, doi: 10.1016/j.mattod.2021.11.019.

[63] A. Deschamps et Y. Brechet, « Influence of predeformation and agEing of an Al–Zn–Mg alloy—II. Modeling of precipitation kinetics and yield stress », *Acta Materialia*, vol. 47, nº 1, p. 293-305, déc. 1998, doi: 10.1016/S1359-6454(98)00296-1.

[64] R. Li, M. Wang, Z. Li, P. Cao, T. Yuan, et H. Zhu, « Developing a high-strength Al-Mg-Si-Sc-Zr alloy for selective laser melting: Crack-inhibiting and multiple strengthening mechanisms », *Acta Materialia*, vol. 193, p. 83-98, juill. 2020, doi: 10.1016/j.actamat.2020.03.060.

[65] W. Lefebvre, N. Masquelier, J. Houard, R. Patte, et H. Zapolsky, « Tracking the path of dislocations across ordered Al3Zr nano-precipitates in three dimensions », *Scripta Materialia*, vol. 70, p. 43-46, janv. 2014, doi: 10.1016/j.scriptamat.2013.09.014.

[66] A. J. Ardell, « Precipitation hardening », *Metall Trans A*, vol. 16, nº 12, p. 2131-2165, déc. 1985, doi: 10.1007/BF02670416.

[67] C. B. Fuller, D. N. Seidman, et D. C. Dunand, « Mechanical properties of Al(Sc,Zr) alloys at ambient and elevated temperatures », *Acta Materialia*, vol. 51, nº 16, p. 4803-4814, sept. 2003, doi: 10.1016/S1359-6454(03)00320-3.

[68] S. Thangaraju, M. Heilmaier, B. S. Murty, et S. S. Vadlamani, « On the Estimation of True Hall-Petch Constants and Their Role on the Superposition Law Exponent in Al Alloys », *Adv. Eng. Mater.*, vol. 14, nº 10, p. 892-897, oct. 2012, doi: 10.1002/adem.201200114.

APPENDIX A

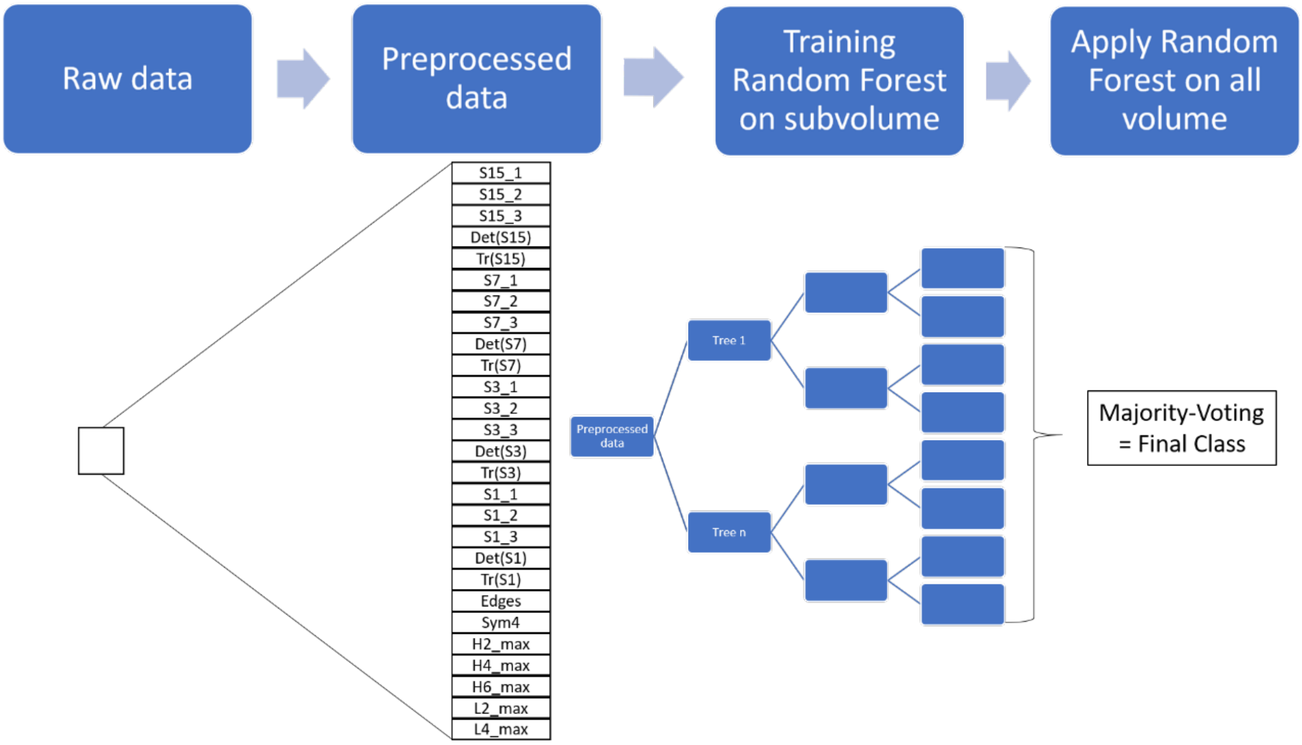

Figure A. 1 First row: work flow of the AI allowing the segmentation of the 3D images obtanined from nano-CT. Second row: illustration of the work flow for one given pixel.

The initial raw data are 8-bit images with a voxel size of 88.4 nm. Each nano-CT scan has the following dimensions in pixels: 2560×2560×2160 (height). The height is aligned with the build direction.

Pre-processing of the raw data consists of using filters to extract features characteristic of the close environment of each pixel. To be representative of the local environment at different scales, different sizes of kernel (1,3,7,15 voxels) have been used. The environment of the voxel is summarized by one vector containing 27 features (**Figure A. 1**). In this vector, S corresponds to the structure tensor, H represents the Hessian tensor, and L the Laplacian one. The number written after the letter corresponds to the size of the kernel. The last number is used to differentiate eigenvalues. For example, S15_1 in **Figure A. 1** is the eigenvalue of one of the structure tensors obtained with a kernel size of 15. If the last number is replaced by max, it means that the highest eigenvalue has been selected. For example, H2_max represents the highest eigenvalue of the Hessian tensor with a kernel size of 2.
Det(X) and Tr(X) correspond respectively to the determinant and the trace of the tensor X. For example, Det(S15) is the determinant of the structure tensor obtained with a kernel size of 15.
Finally, two other values, edges and sym4, obtained with a symmetry plugin in the Fiji software have been selected to be able to detect edges or symmetry in the microstructure using a kernel size of 4.

After this preprocessing the random forest illustrated in the second row in **Figure A. 1**, is trained on subvolumes in which the microstructure has been segmented manually. When the accuracy is above 0.98, the random forest is applied to the whole volume. It means for each pixel, the vector containing values associated with the 27 features described above is passed throughout the random forest leading to a “vote” of each tree in the random forest. The class with the highest number of votes is considered the most probable.

APPENDIX B

All the constants used to estimate the different strengthening contributions to the yield strength in the FZ and CZ are given in **Table B. 1**.

Parameters			**References**
σ_0 (MPa)	Friction stress of Al	10	[63]
k_y (MPa.m$^{1/2}$)	Hall Petch parameter	0.14	[64]
M	Taylor factor for a random texture	3.06	
v	Poisson ratio of Al	0.345	[65]
G_{Al} (GPa)	Shear modulus of Al	25.4	[65]
G_{Al3Zr}	Shear modulus of L1$_2$-Al$_3$Zr nanoprecipitates	57	[65]
ΔG	Shear modulus mismatch between Al and L1$_2$-Al$_3$Zr	31.6	
b (nm)	Burgers vector of Al	0.286	[65]
$w = 5b$ (nm)	Interaction force parameter	1.430	
ε_{Mn} (%)	Misfit strain for Mn	-4.20	[48]
ε_{Zr} (%)	Misfit strain for Zr	1.23	[48]
ε_{Ni} (%)	Misfit strain for Ni	-1.94	[48]
ε_{Cu} (%)	Misfit strain for Cu	-3.13	[48]
α_{Coh}	Constant for coherency strenghtening	2.6	[66]
θ	Constrained lattice parameter mismatch at RT ≈ (2/3) δ	0.005	[67]
δ (%)	Lattice parameter misfit between Al and L1$_2$-Al$_3$Zr	1	
m	Constant for modulus strengthening	0.85	[66]

Table B. 1. Summary of all the constants used to estimate the various strengthening contributions to the yield strength in the FZ and CZ.

The grain boundary strengthening contribution in region i = FZ, CZ was calculated using equation (B-1):

$$\Delta\sigma_{GB}^{i} = \sigma_0 + k_y/d_i^{-0.5} \qquad \text{(B-1)}$$

with $\sigma_0 = 10$ MPa the friction stress of pure Al, $d_{FZ} = 0.5\ \mu m$, $d_{CZ} = 10\ \mu m$, and a Hall-Petch constant k_y = 0.14 MPa.m$^{1/2}$ [62]. Note that k_y between 0.06 [68] and 0.17 [27] can be found in the literature. This can cause important variations in the estimation of the grain boundary strengthening. Here, we took k_y within the range of values found in the literature.

The solid solution strengthening contribution in region i = FZ, CZ was estimated using equation (B-2):

$$\Delta\sigma_{SS}^{i} = M\left(\frac{3}{8}\right)^{2/3}\left(\frac{1+\nu}{1-\nu}\right)^{4/3}\left(\frac{w}{b}\right)^{1/3} G \times \sum_j \left|\varepsilon_j\right|^{4/3} c_j^{2/3} \qquad \text{(B-2)}$$

with M the Taylor factor, v the Poisson ratio, G the shear modulus of aluminium, b aluminium, b the Burgers vector of FCC Al, w a material parameter called the interaction force range (here we took $w = 5b$ as proposed in [48]), ε_j the misfit strain for the solute j = Mn, Zr, Ni, Cu calculated from the first principles [48], and c_j the concentration of solute j in solid solution measured respectively in the CZ and FZ using atom probe tomography in [36] and given in **Table B. 2**.

		FZ	**CZ**
SR	c_{Mn}	1.64	1.77
	c_{Ni}	0.03	0.02
	c_{Cu}	0.04	0.07
	c_{Zr}	0.37	0.41
SR + 400°C/1h	c_{Mn}	0.71	0.69
	c_{Ni}	0.01	0.03
	c_{Cu}	0.16	0.17
	c_{Zr}	0.23	0.20

Table B. 2. Composition of the aluminium matrix in %at in the FZ and CZ measured by atom probe tomography in [36] in the SR and SR+400°C/1h sample.

The precipitation strengthening contribution brought by the spherical $L1_2$-Al_3Zr precipitates in region i = FZ, CZ was found to be governed by coherency and modulus effects [36] and was thus calculated using equation (B-3):

$$\Delta\sigma_P^i = \Delta\sigma_{Coh}^i + \Delta\sigma_{Mod}^i \tag{B-3}$$

with

$\Delta\sigma_{Coh}^i = M\alpha_{Coh}(G\theta)^{\frac{3}{2}}\left(\frac{\langle R\rangle^i f_v^i}{0.5Gb}\right)^{\frac{1}{2}}$ where G is the shear modulus of the matrix FCC Al, α_{Coh} is a constant, θ is the constrained lattice parameter mismatch at RT taken here ≈ $(2/3)\delta$ where δ is the lattice parameter mismatch, $\langle R\rangle^i$ and f_v^i are respectively the average size and volume fraction of the nanoprecipitates in region i = FZ, CZ. The average size of the $L1_2$-Al_3Zr nanoscale precipitates was considered equal in both FZ and CZ: $\langle R\rangle^{FZ} = \langle R\rangle^{CZ} = 1.3\ \text{nm}$ (measured by SAXS in [36]). The volume fraction of precipitates in the FZ and CZ were taken respectively equal to $f_v^{FZ} = 0.4\%$, and $f_v^{CZ} = 0.8\%$ as deduced from APT measurements in [36].

$\Delta\sigma_{Mod}^i = 0.0055M(\Delta G)^{\frac{3}{2}}\left(\frac{2f_v^i}{Gb^2}\right)^{\frac{1}{2}} b\left(\frac{\langle R\rangle^i}{b}\right)^{\left(\left(\frac{3m}{2}\right)-1\right)}$ where ΔG is the difference in shear modulus between the matrix FCC Al and the $L1_2$-Al_3Zr nanoprecipitates and m a constant.

VIDEO 'STILLS'

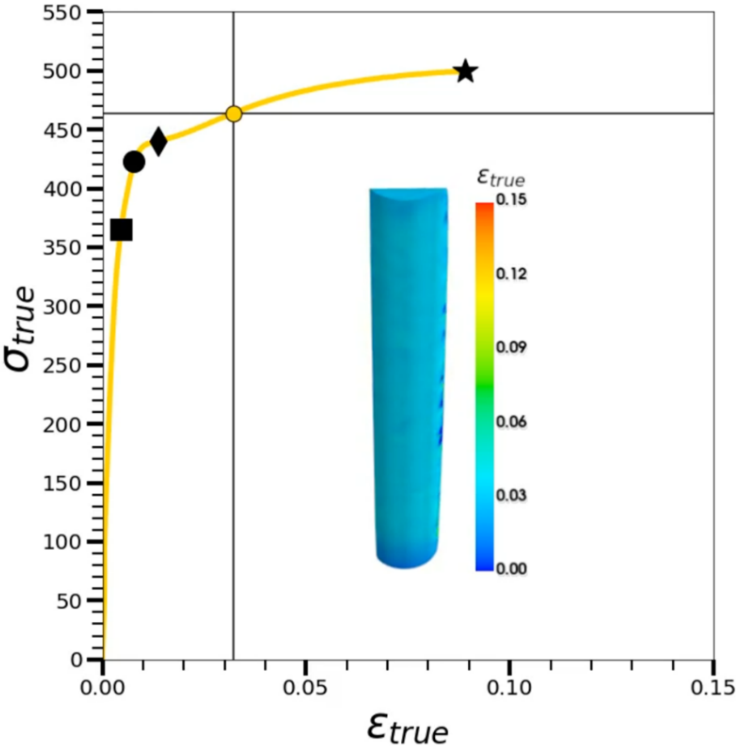

Video 1. *Evolution of the macroscale strain distribution using DIC during tensile deformation of the SR+400°C/1h sample.*

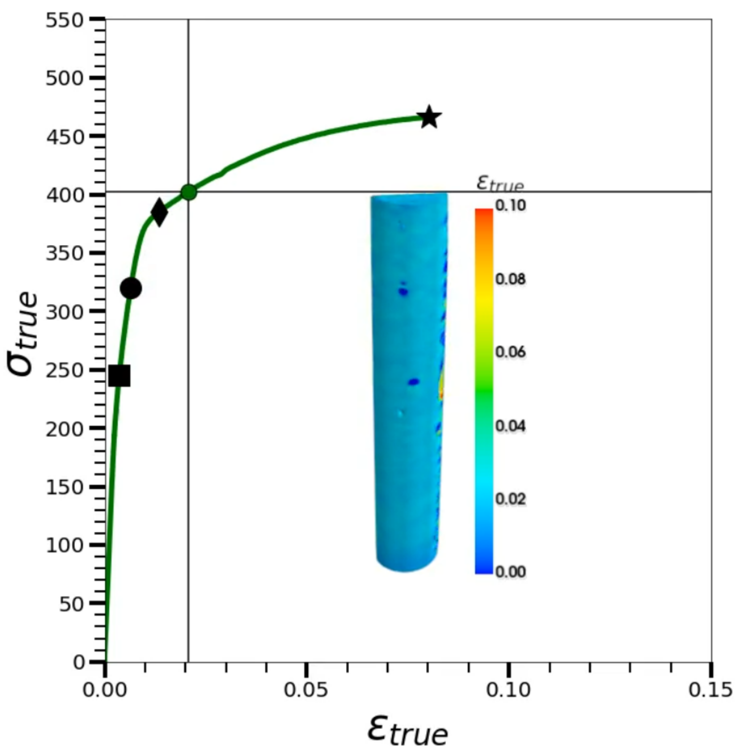

Video 2. *Evolution of the macroscale strain distribution determined using DIC during tensile deformation of the SR sample.*

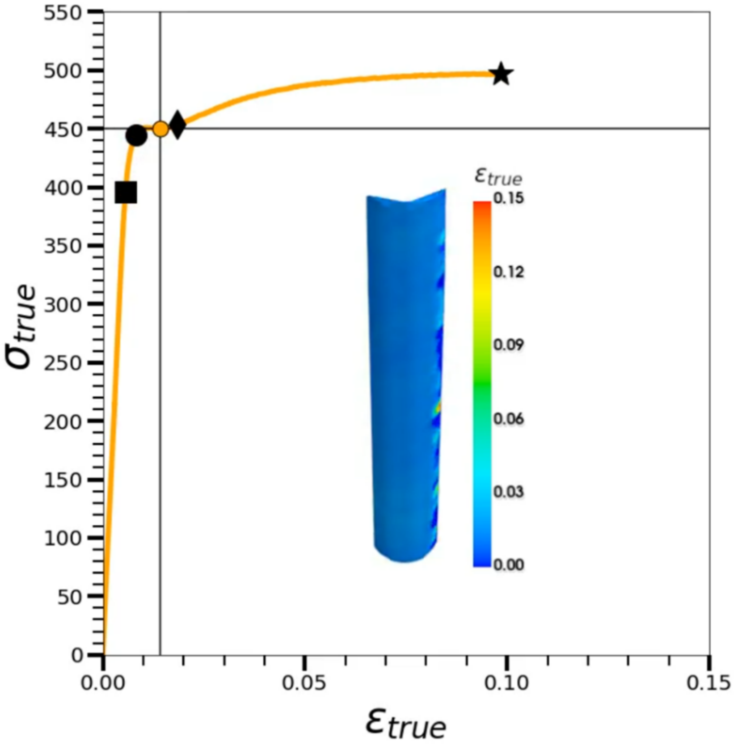

Video 3. *Evolution of the macroscale strain distribution determined using DIC during tensile deformation of the SR+400°C/4h sample.*

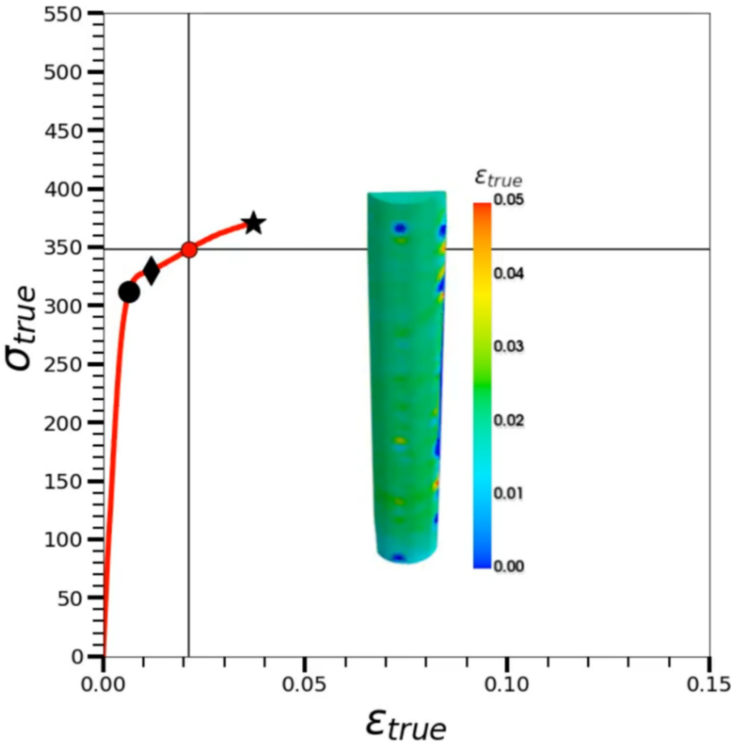

Video 4. *Evolution of the macroscale strain distribution determined using DIC during tensile deformation of the SR+400°C/96h sample.*

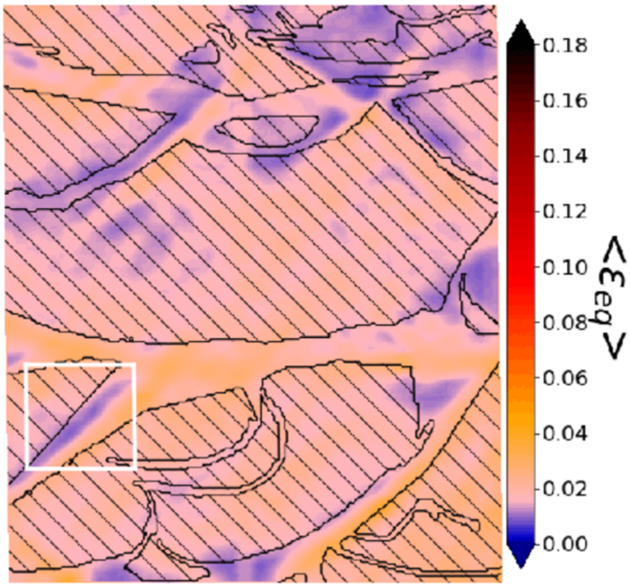

Video 5. *Evolution of the microscale strain distribution determined using DIC during tensile deformation of the SR+400°C/1h sample (build platform = 100°C).*

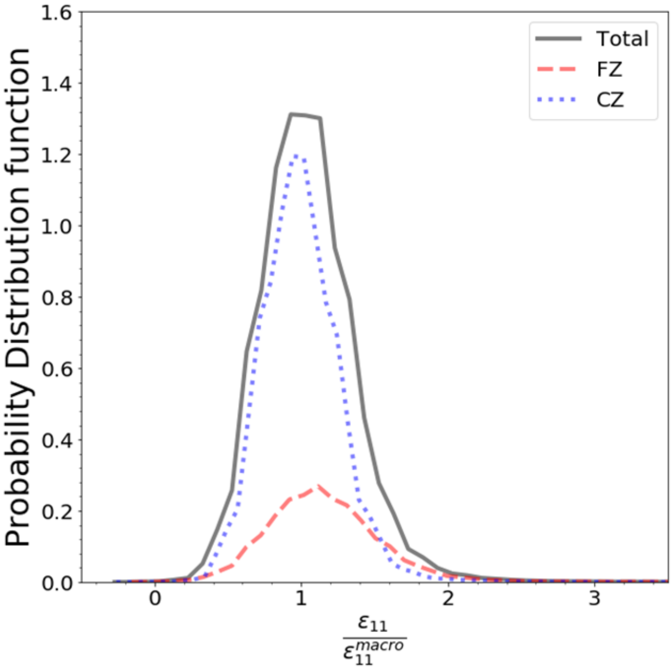

Video 6. Evolution of the total strain distribution (in gray) and in the FZ (in red) and CZ (in blue) during tensile deformation-of the SR+400°C/1h sample (build platform = 100°C).

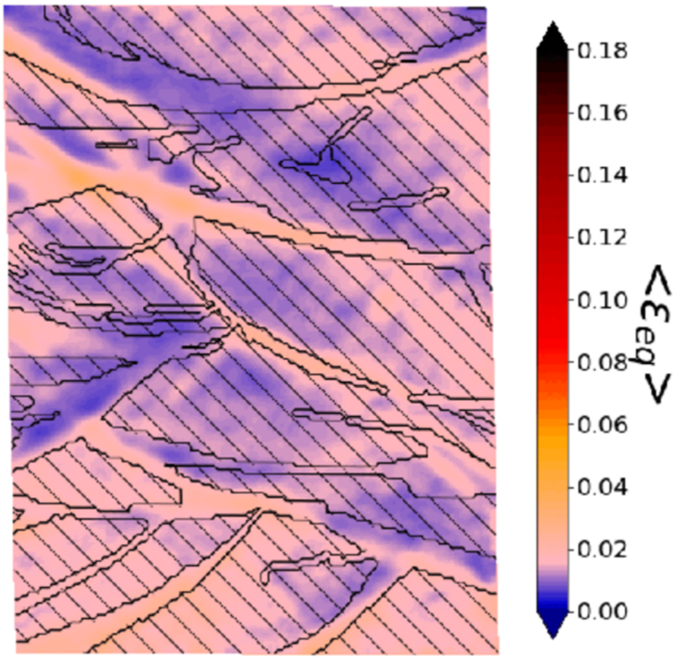

Video 7. *Evolution of the microscale strain distribution determined using DIC during tensile deformation of the SR sample (build platform = 100°C).*

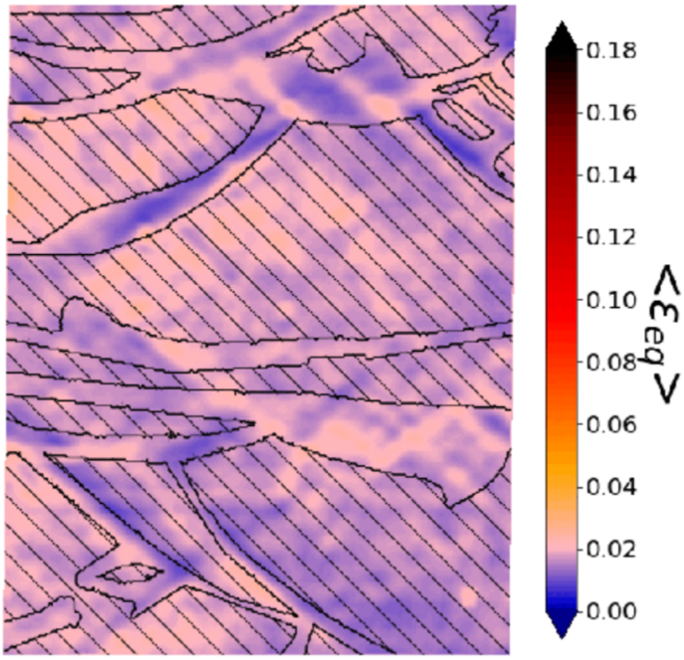

Video 8. *Evolution of the microscale strain distribution determined using DIC during tensile deformation of the SR+400°C/4h sample (build platform = 100°C).*

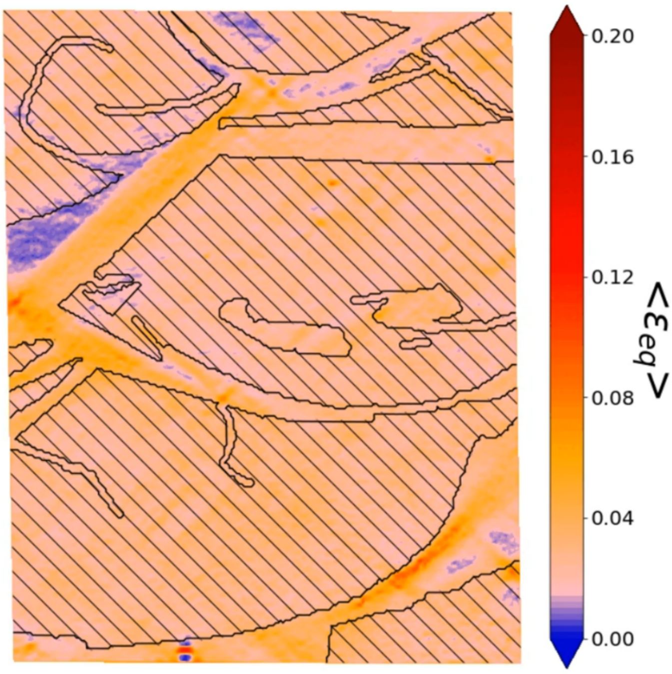

Video 9. *Evolution of the microscale strain distribution determined using DIC during tensile deformation of the SR+400°C/1h sample (build platform = 100°C).*

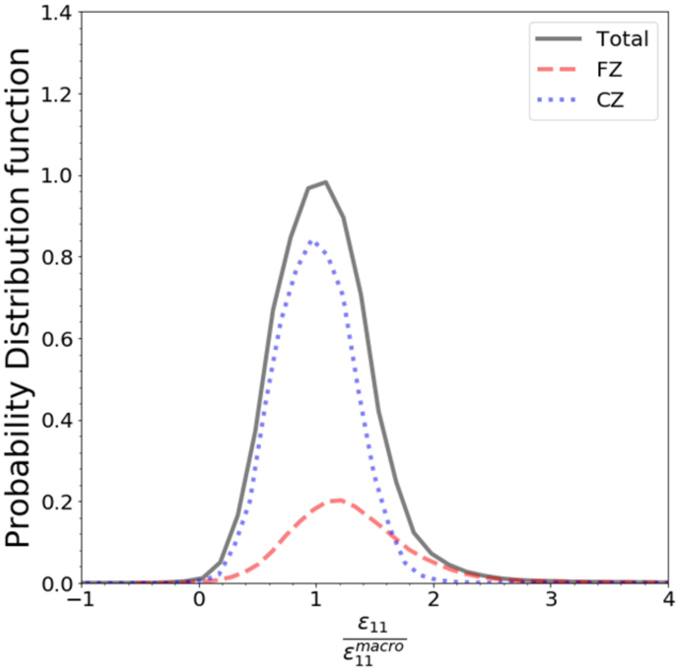

Video 10. *Evolution of the total strain distribution (in gray) and in the FZ (in red) and CZ (in blue) during tensile deformation-of the SR+400°C/1h sample (build platform = 200°C).*

SUPPLEMENTARY MATERIALS

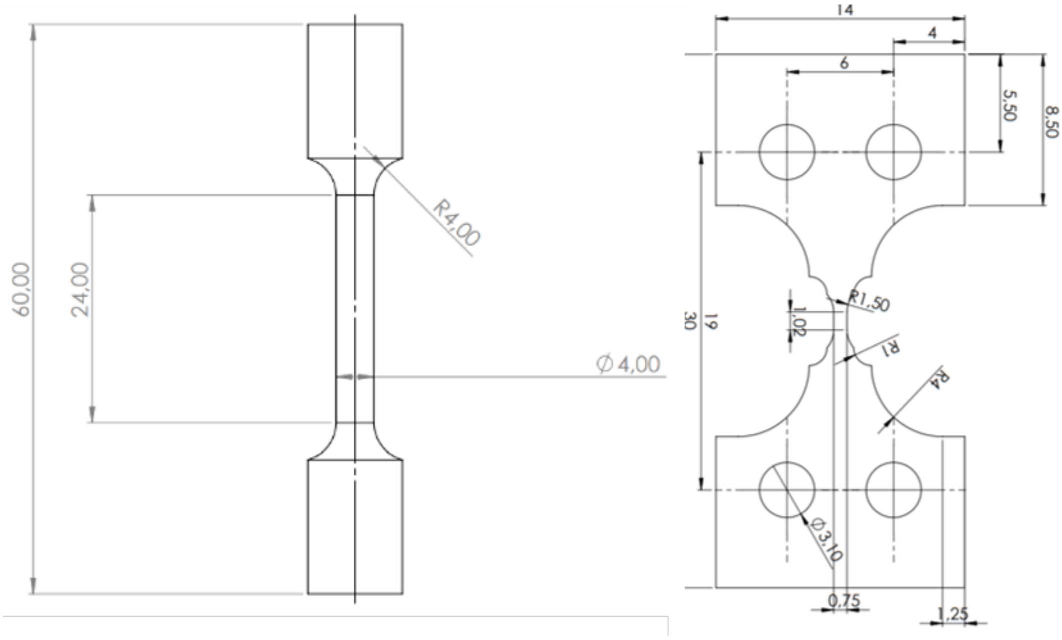

Figure S 1: Geometry of the tensile specimens for (right) the macroscopic tensile test and (b) the in-situ tensile test. Dimensions are given in mm.

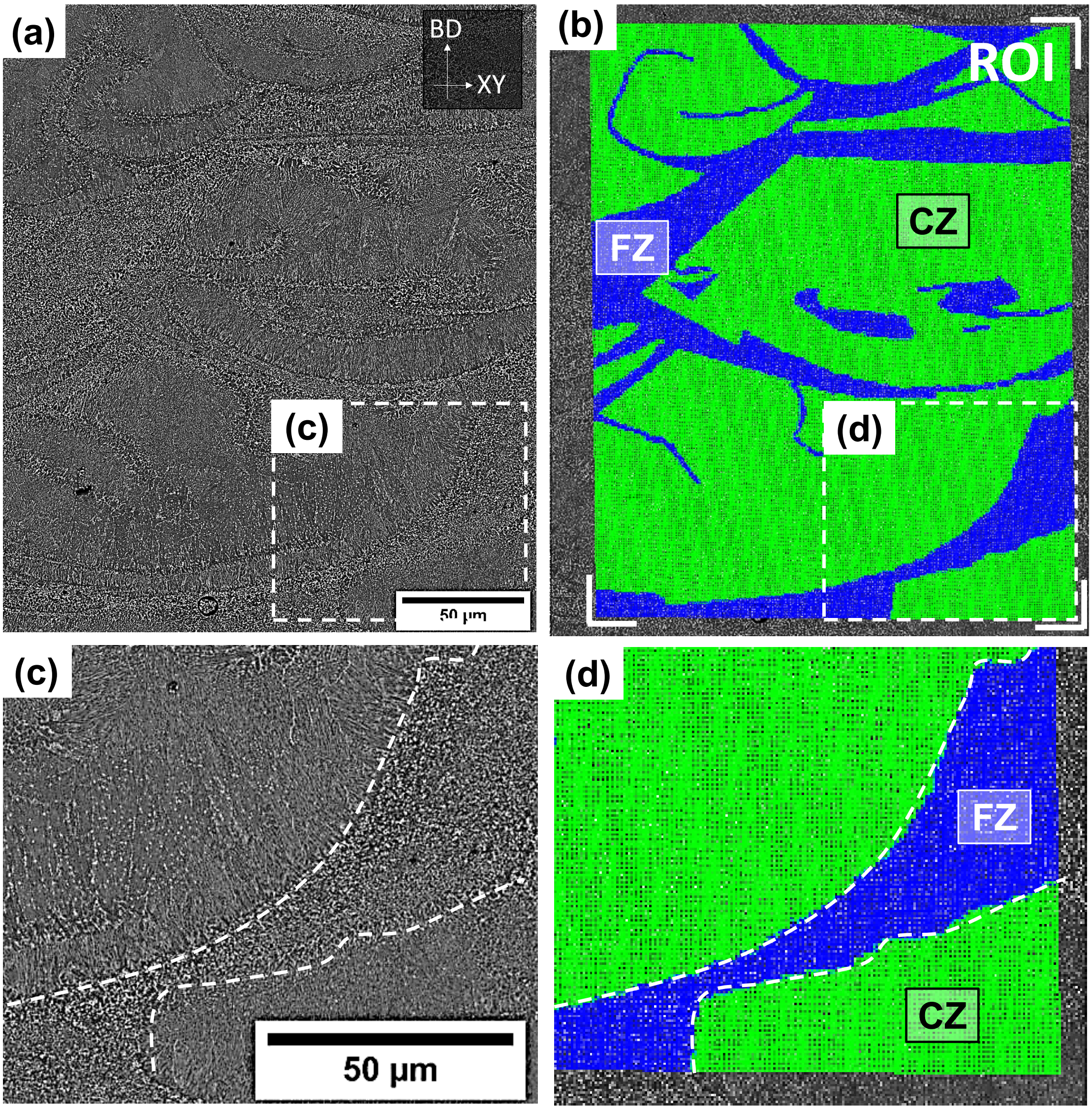

Figure S 2. (a) High-definition SEM-BSE image showing in (b) the region of interest (ROI) selected for microscale DIC measurement in the SR+400°C/1h sample where the DIC subsets belonging to the FZ and CZ are respectively displayed in blue and green. (c) and (d) Enlarged views of the region highlighted with a white dashed line in (a) and (b).

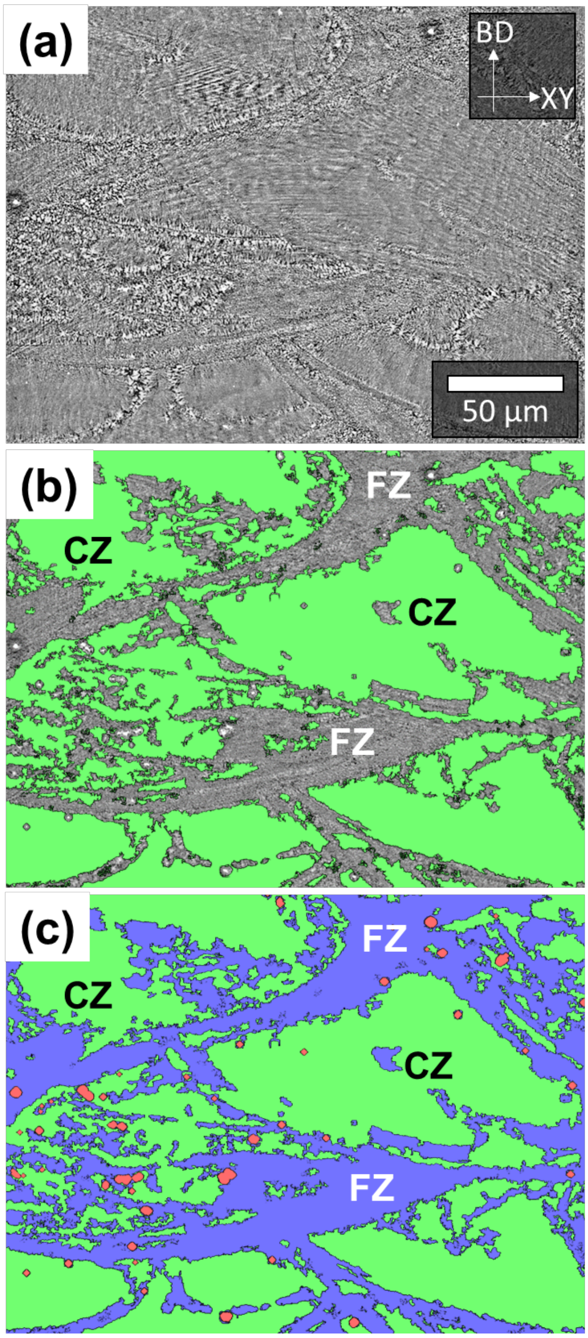

Figure S 3. Example of a 2D cross-section extracted from the 3D image: (a) grayscale image resulting from nano-CT; (b) Result of the machine learning-assisted segmentation with the CZ displayed in green; (c) Result of the machine learning-assisted segmentation with the CZ in green and FZ in blue. Pores are displayed in red.

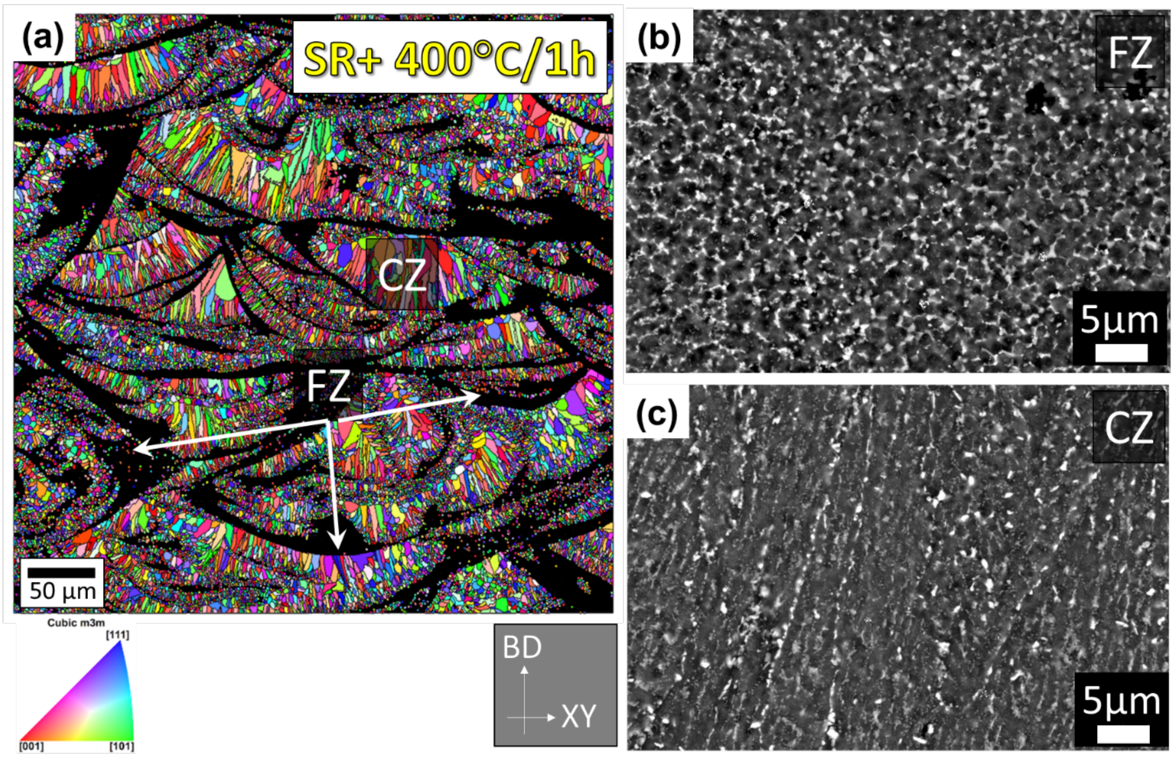

Figure S 4. Overview of the microstructure in the SR+400°C/1h sample. (a) EBSD-IPF map of aluminium revealing the bimodal grain structure with fine equiaxed zones (FZ, mostly in black) and zones consisting of coarser columnar grains (CZ). Typical examples of BSE images taken respectively in the (b) FZ, and (c) CZ of the SR+400°C/1h sample. Intermetallic particles appear in bright contrast.

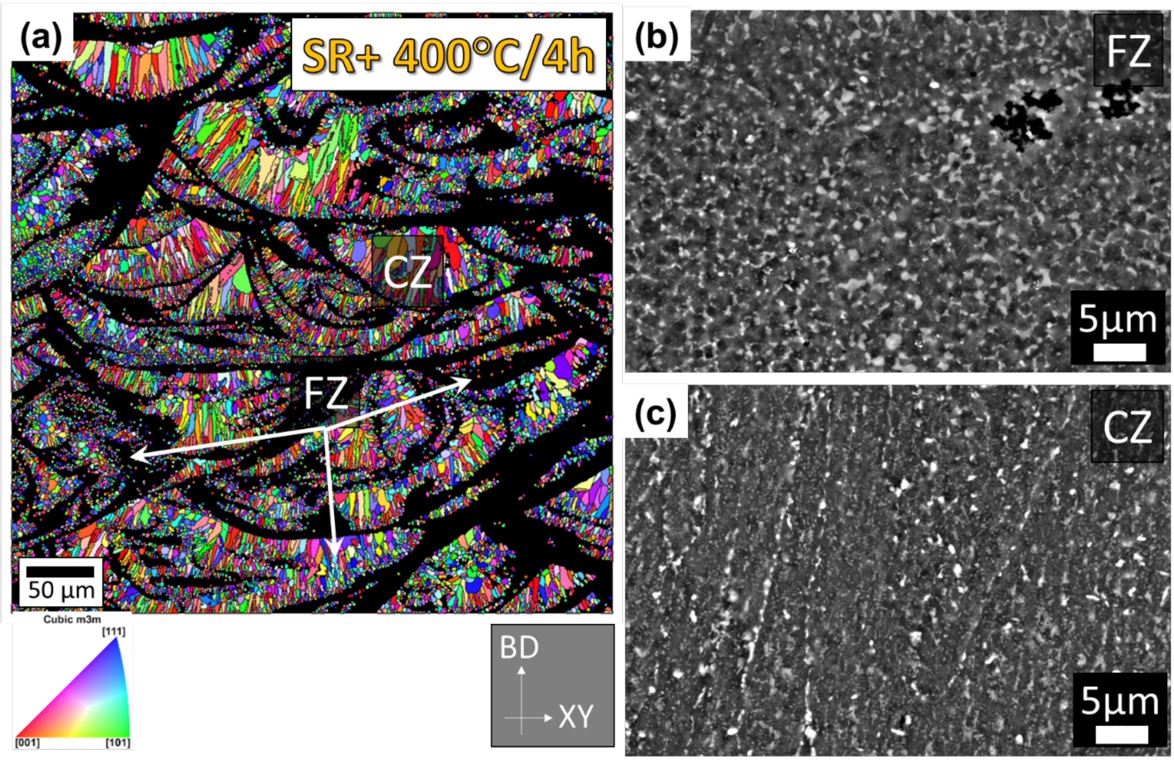

Figure S 5. Overview of the microstructure in the SR+400°C/4h sample. (a) EBSD-IPF map of aluminium revealing the bimodal grain structure with fine equiaxed zones (FZ, mostly in black) and zones consisting of coarser columnar grains (CZ). Typical examples of BSE images taken respectively in the (b) FZ, and (c) CZ of the SR+400°C/4h sample. Intermetallic particles appear in bright contrast.

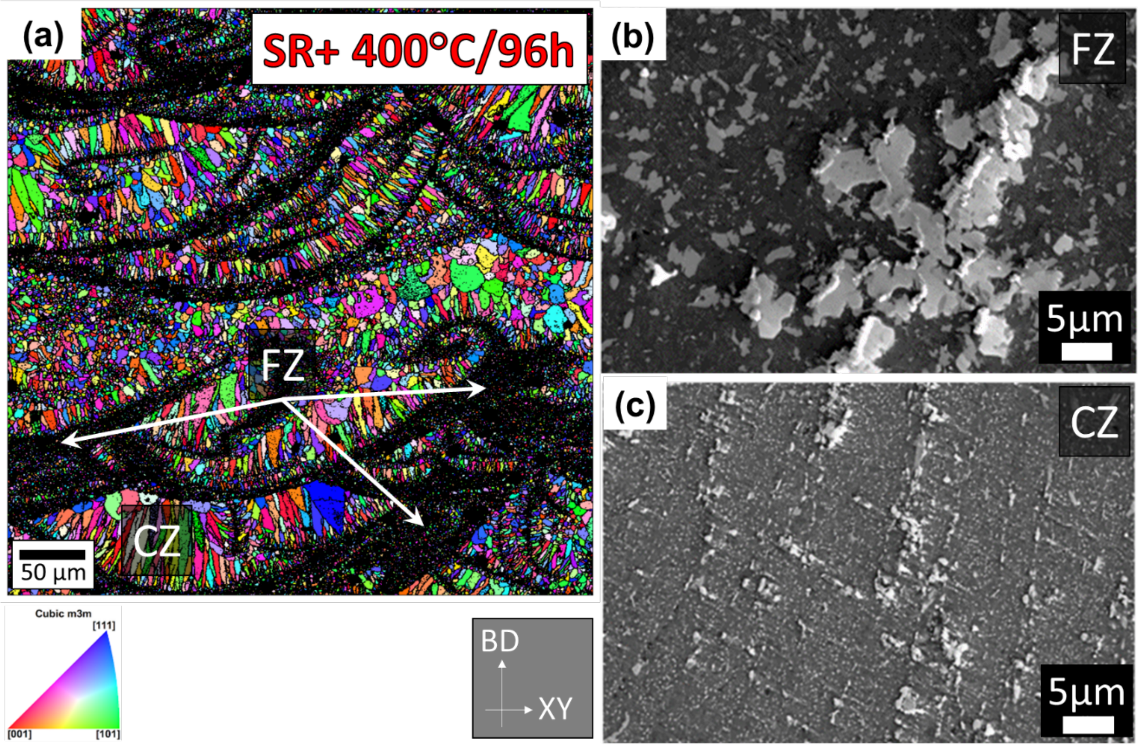

Figure S 6. Overview of the microstructure in the SR+400°C/96h sample. (a) EBSD-IPF map of aluminium revealing the bimodal grain structure with fine equiaxed zones (FZ, mostly in black) and zones consisting of coarser columnar grains (CZ). Typical examples of BSE images taken respectively in the (b) FZ, and (c) CZ of the SR+400°C/96h sample. Intermetallic particles appear in bright contrast.

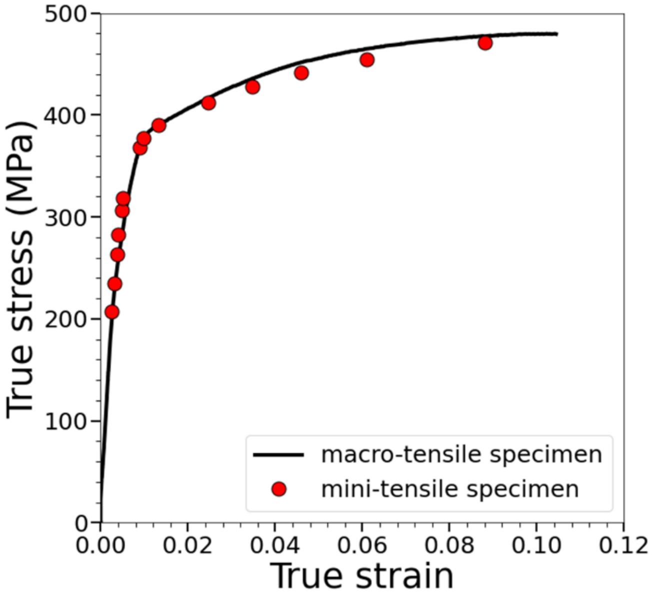

Figure S 7. Comparison between the tensile response recorded using respectively macro and micro tensile specimens: example taken from the SR conditions. Full lines correspond to a test run using macro-tensile specimens. Red points are associated with the tensile response recorded using a mini-tensile specimen.

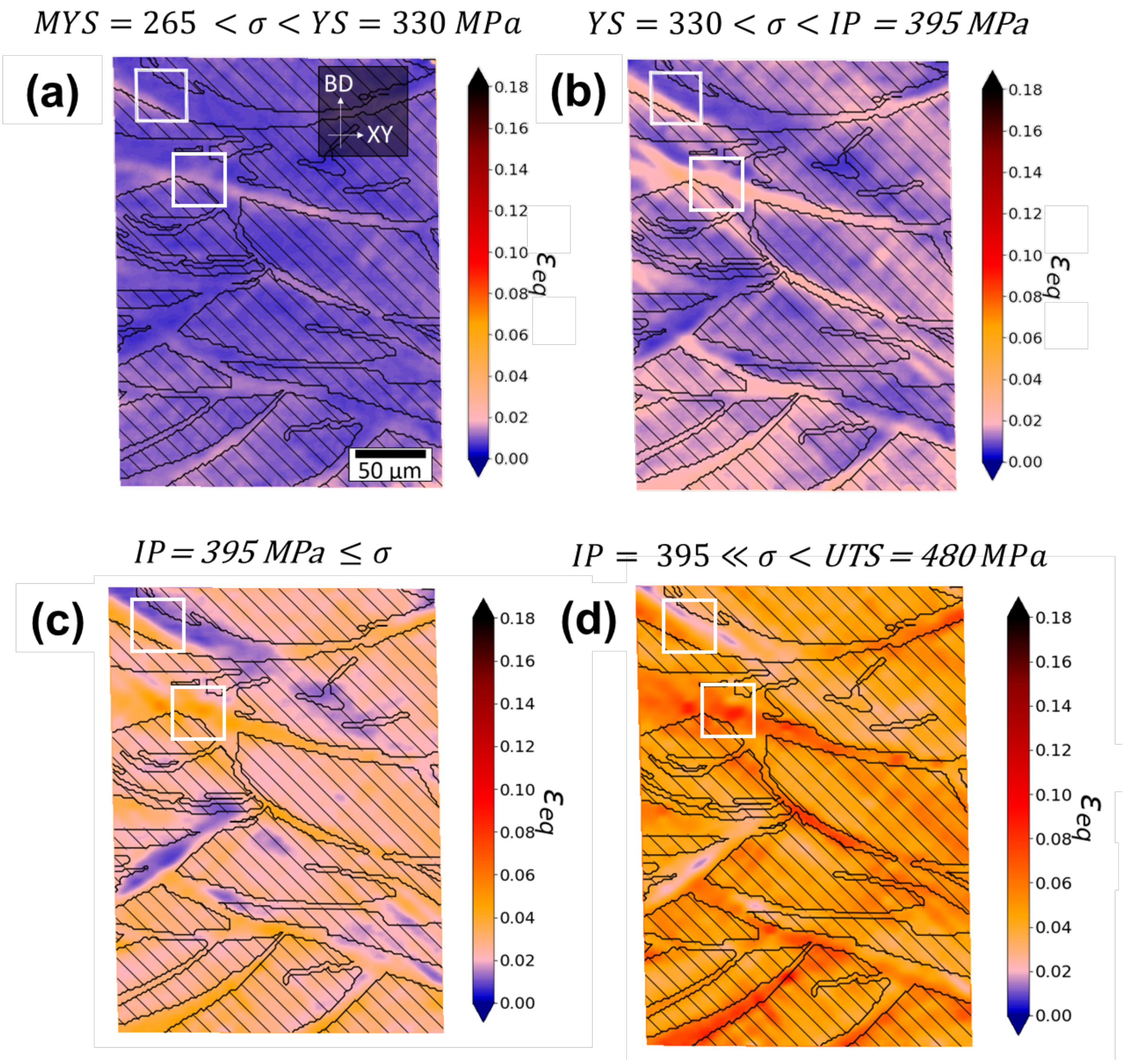

$MYS = 265 < \sigma < YS = 330\ MPa$

$YS = 330 < \sigma < IP = 395\ MPa$

$IP = 395\ MPa \leq \sigma$

$IP = 395 \ll \sigma < UTS = 480\ MPa$

Figure S 8. Microscale equivalent Von Mises strain fields determined in the SR for different levels of macroscopic tensile stress: (a) MYS < σ < YS; (b) YS < σ < IP; (c) IP ≤ σ ; IP << σ < UTS. The black lines correspond to the interfaces between FZ and CZ. The CZs are identified as the hatched areas. White boxes are associated with regions where the propagation of deformation bands can be observed.

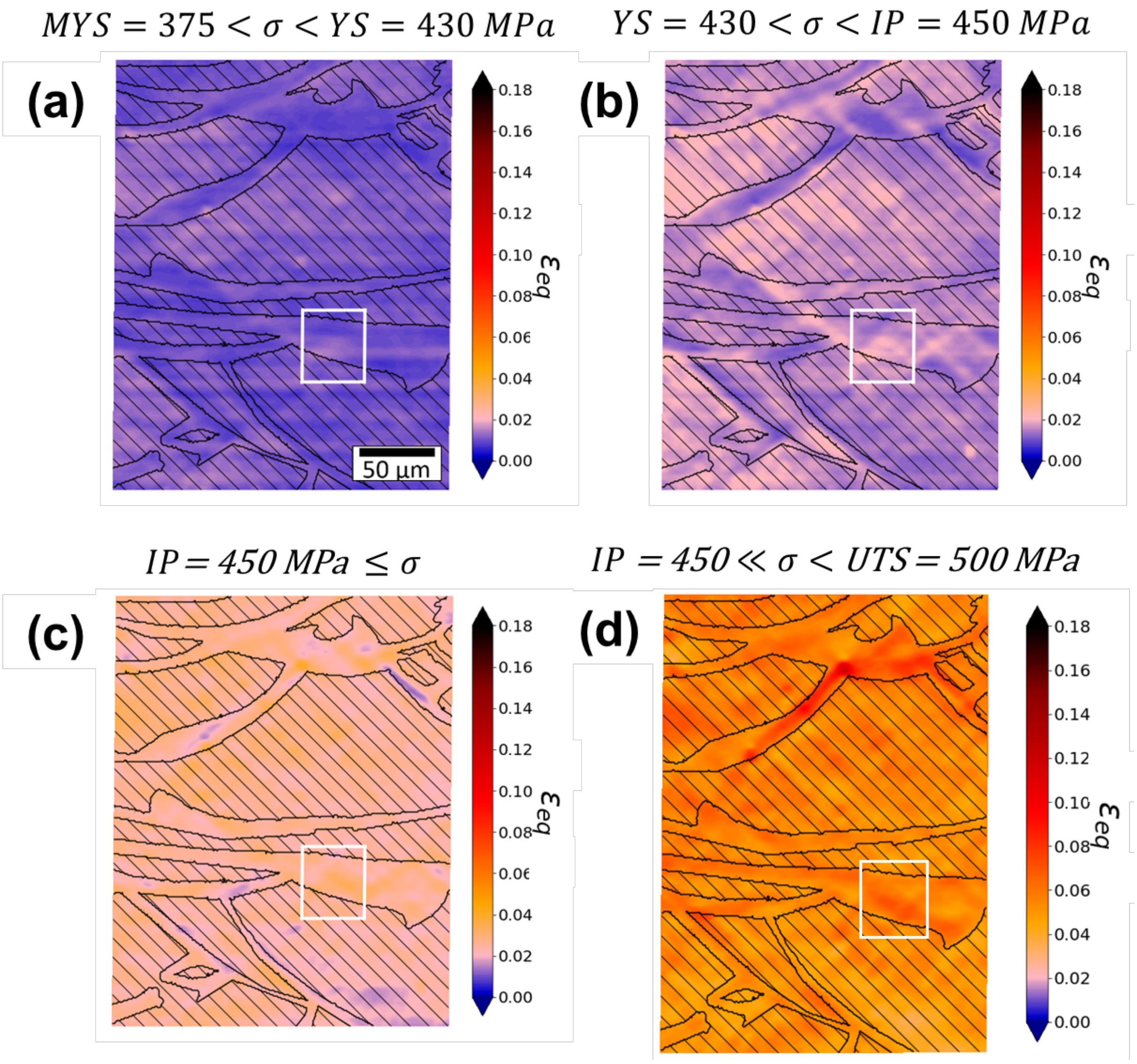

$MYS = 375 < \sigma < YS = 430\ MPa$

$YS = 430 < \sigma < IP = 450\ MPa$

$IP = 450\ MPa \leq \sigma$

$IP = 450 \ll \sigma < UTS = 500\ MPa$

Figure S 9. Microscale equivalent Von Mises strain fields determined in the SR+400°C/4h sample for different levels of macroscopic tensile stress: (a) MYS < σ < YS; (b) YS < σ < IP; (c) IP ≤ σ; IP << σ < UTS. The black lines correspond to the interfaces between FZ and CZ. The CZs are identified as the hatched areas. White boxes are associated with regions where the propagation of deformation bands can be observed.

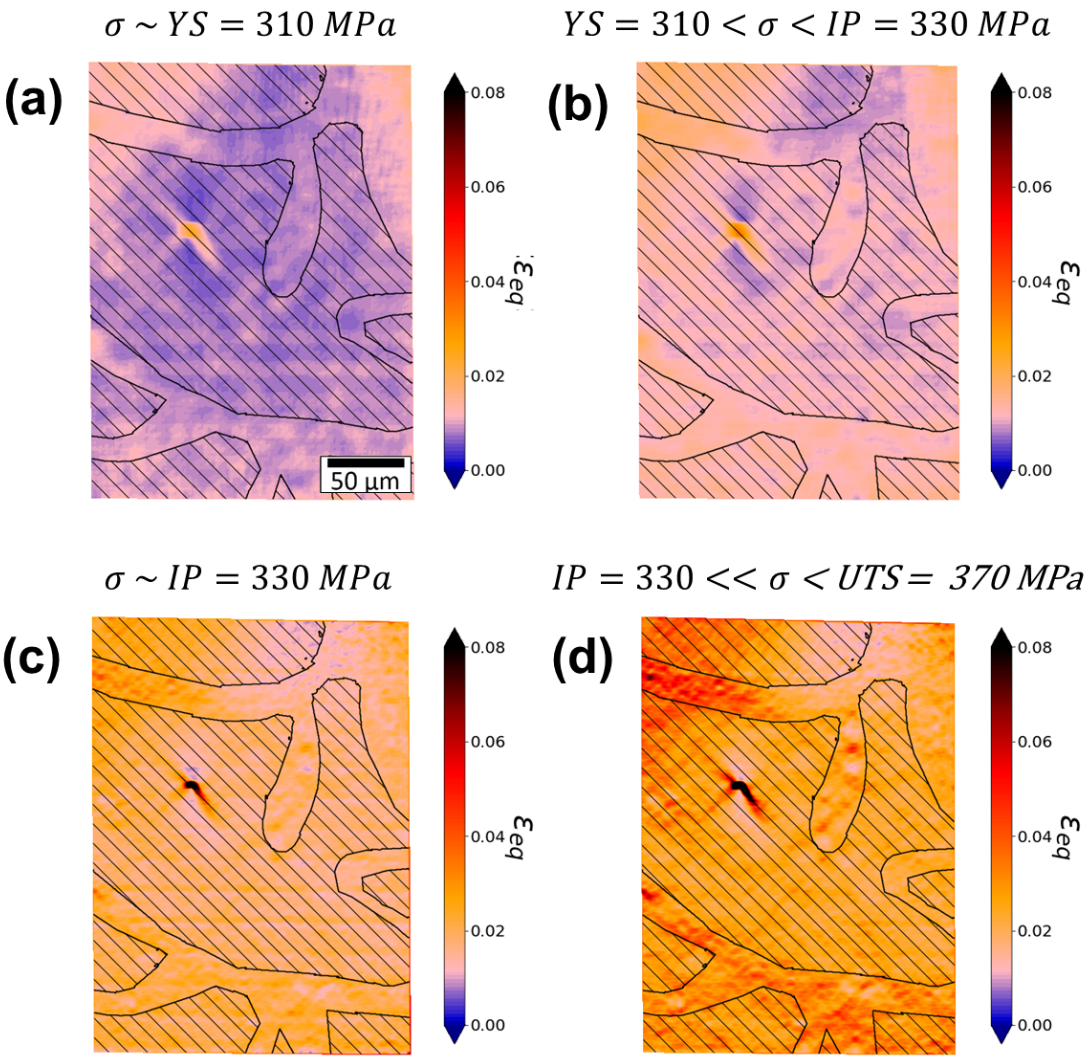

Figure S 10. Microscale strain fields determined in the SR+400°C/96h sample for different levels of macroscopic tensile stress: (a) σ ~ YS = 310 MPa; (b) YS = 310 < σ < IP = 330 MPa; (c) σ ~ IP = 330 MPa; (d) IP = 330 << σ < UTS = 370 MPa. The black lines correspond to the interfaces between FZ and CZ. The CZs are identified as the hatched areas.

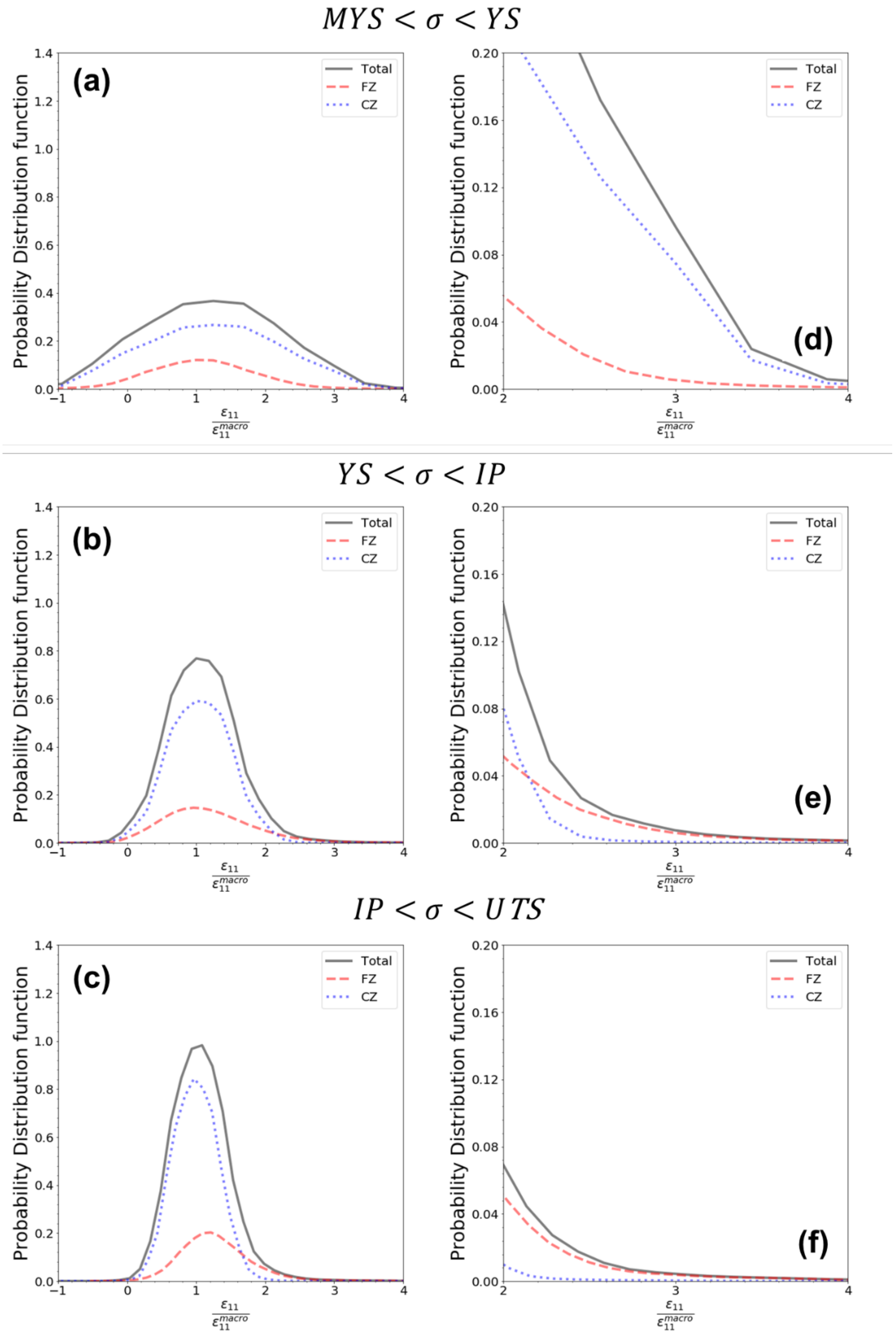

Figure S 11. Evolution of the probability distribution functions of the normalized local tensile strain in the FZ, CZ and entire ROI during tensile straining in the SR+400°C/1h sample (build platform preheated at 200°C) along with zoom-in views of the tail of the strain distributions: (a,d) MYS < σ < YS; (b,e) YS < σ < IP; and (c,f) IP < σ < UTS.